

## SPECTRAL STATE EVOLUTION OF 4U 1820–30: THE STABILITY OF THE SPECTRAL INDEX OF THE COMPTONIZATION TAIL

LEV TITARCHUK<sup>1,2,3</sup>, ELENA SEIFINA<sup>4</sup>, AND FILIPPO FRONTERA<sup>1</sup>

<sup>1</sup> Dipartimento di Fisica, Università di Ferrara, Via Saragat 1, I-44122 Ferrara, Italy;  
[titarchuk@fe.infn.it](mailto:titarchuk@fe.infn.it), [lev@milkyway.gsfc.nasa.gov](mailto:lev@milkyway.gsfc.nasa.gov), [frontera@fe.infn.it](mailto:frontera@fe.infn.it)

<sup>2</sup> George Mason University, Fairfax, VA 22030, USA

<sup>3</sup> Goddard Space Flight Center, NASA, Code 663, Greenbelt, MD 20770, USA

<sup>4</sup> Moscow M.V. Lomonosov State University/Sternberg Astronomical Institute, Universitetsky Prospect 13,  
Moscow 119992, Russia; [seif@sai.msu.ru](mailto:seif@sai.msu.ru)

Received 2012 July 27; accepted 2013 February 8; published 2013 April 8

### ABSTRACT

We analyze the X-ray spectra and their timing properties of the compact X-ray binary 4U 1820–30. We establish spectral transitions in this source seen with *BeppoSAX* and the *Rossi X-ray Timing Explorer* (*RXTE*). During the *RXTE* observations (1996–2009), the source was in the soft state approximately  $\sim 75\%$  of the time making the lower banana and upper banana transitions combined with long-term low–high state transitions. We reveal that all of the X-ray spectra of 4U 1820–30 are fit by a combination of a thermal (Blackbody) component, a Comptonization component (COMPTB), and a Gaussian-line component. Thus, using this spectral analysis, we find that the photon power-law index  $\Gamma$  of the Comptonization component is almost unchangeable ( $\Gamma \sim 2$ ), while the electron temperature  $kT_e$  changes from 2.9 to 21 keV during these spectral events. We also establish that for these spectral events the normalization of the COMPTB component (which is proportional to the mass accretion rate  $\dot{M}$ ) increases by a factor of eight when  $kT_e$  decreases from 21 keV to 2.9 keV. Previously, this index stability effect was also found analyzing X-ray data for the Z-source GX 340+0 and for the atolls 4U 1728–34 and GX 3+1. Thus, we can suggest that this spectral stability property is a spectral signature of an accreting neutron star source. On the other hand, in a black hole binary  $\Gamma$  monotonically increases with  $\dot{M}$  and ultimately its value saturates at large  $\dot{M}$ .

**Key words:** accretion, accretion disks – black hole physics – radiation mechanisms: non-thermal – stars: individual (4U 1820–30)

**Online-only material:** color figures

### 1. INTRODUCTION

Accreting neutron stars (NSs) can be observationally classified into two distinct categories using a color–color diagram (CCD). These two categories, atolls and Z sources, are based on their different CCD forms when the source undergoes spectral and luminosity changes. Along with this phenomenological difference between atolls and Z-sources in terms of the CCD, there are important X-ray spectral and timing characteristics that are essentially different for these types of NS low-mass X-ray binaries (LMXBs). The main observational difference between these types is the specific range of luminosity changes. The atolls are observed when their luminosity changes from 0.01 up to 0.5 of the Eddington limit  $L_{\text{Edd}}$  (see Christian & Swank 1997; Ford et al. 2000), while Z-sources are seen when the resulting luminosity is near the Eddington regime (e.g., Seifina et al. 2013). In this paper, we present our analysis of the peculiar atoll 4U 1820–30, which is a bright atoll source in terms of its luminosity and, at the same time, is a typical atoll source in terms of its timing evolution. On the other hand, during the bright phase, 4U 1820–30 is as bright as a subclass of persistent bright atolls (GX 13+1, GX 9+1, GX 9+9, and GX 3+1), but 4U 1820–30 shows a larger range of luminosity and demonstrates all states in terms of CCD (from the island to banana states). The aforementioned bright atolls are only seen in the banana state (e.g., Hasinger & van der Klis 1989).

Furthermore, 4U 1820–30 has a maximal luminosity of about 0.5  $L_{\text{Edd}}$  and thus it adjoins the luminosity range of Z-sources. Also, 4U 1820–30 shows Type-I X-ray bursts and characteristic timing features of a typical atoll demonstrating

an evolution of band-limited noise (BLN), very low frequency noise (VLFN) components, and low-frequency quasi-periodic oscillations (LFQPOs, in the 20–40 Hz range) when it evolves from the banana state to the island state. However, unlike the other atolls, 4U 1820–30 exhibits LFQPOs with frequencies near 6 Hz during the banana state (Wijnands et al. 1999; also see Section 6.2 in this paper), which are usually seen in Z-sources during the normal branch. Thus, 4U 1820–30 combines properties of ordinary and bright atolls and Z-sources in terms of timing and spectral evolution, luminosity, and detection of 6 Hz QPOs.

4U 1820–30 is an LMXB observed at 0''.66 from the center of the NGC 6624 cluster. Grindlay et al. (1976) were the first to identify this source as a Type-I X-ray burst. Kuulkers et al. (2003) estimated the distance  $d = 7.6 \pm 0.4$  kpc to 4U 1820–30, assuming that the peak luminosity equals  $L_{\text{Edd}}$  for a He burst atmosphere. Vacca et al. (1986) estimate the distance to 4U 1820–30 as  $6.4 \pm 0.6$  kpc using the analysis of UV diagrams for NGC 6624. Rappaport et al. (1987) find that the binary system comprises a He white dwarf of mass of  $0.06 \pm 0.08 M_{\odot}$  and NS (with a mass later evaluated by Shaposhnikov & Titarchuk 2004 as  $\sim 1.3 M_{\odot}$ ), orbiting with a period of 11.4 minutes (Stella et al. 1987).

Hasinger & van der Klis (1989) classify 4U 1820–30 as an atoll source. Friedhorsky & Terrell (1984), Simon (2003), and Wen et al. (2006) find that the flux varies between the soft and the hard states (banana and island states, respectively) quasi-periodically with a period of  $\sim 170$  days. These flux variations have been suggested to be related to the tidal effects of a remote third star (Chou & Grindlay 2001; Zdziarski et al. 2007).

*Rossi X-ray Timing Explorer (RXTE)* observations revealed 4U 1820–30 as a prominent source of kilohertz quasi-periodic oscillations (kHz QPO; Smale et al. 1997). X-ray bursts are only observed at low fluxes (e.g., Clark et al. 1977). Furthermore, Cornelisse et al. (2003) and Zhang et al. (1998) find that the observed kHz QPOs correlate with the flux, which probably suggests that these variations are due to a luminosity change caused by a change in the mass accretion rate.

Strohmayer & Bildsten (2004) established that the short ( $\sim 10\text{--}15$  s) Type-I outbursts are due to the unstable thermonuclear burning of a mixture of hydrogen and helium at the bottom of the NS atmosphere. SAS-3 observations showed strong evidence that X-ray bursts can only occur in its low-intensity state (Clark et al. 1977). All bursts observed from 4U 1820–30 indicate that the photosphere expands in radius by a factor of 20. Such an expansion leads to strong softening of the resulting spectrum (see, e.g., Strohmayer & Bildsten 2004). Moreover, a several hour long “superburst” was observed from 4U 1820–30 on 1999 September 9. It is now understood that superbursts can be caused by burning in the carbon ashes produced by Type-I bursts (Strohmayer & Brown 2002).

*Einstein*, EXOSAT, *Ginga*, ASCA, and *BeppoSAX* also observed 4U 1820–30. Many spectral models have been applied to fit the observed X-ray spectra. For example, models that are a sum of a blackbody (BB) with thermal bremsstrahlung or a BB with a power law combined with exponential cutoff (CPL) have been employed. A more detailed model was developed using a Comptonization spectrum by Sunyaev & Titarchuk (1980; see the CompST model in XSPEC) combined with a BB. Note that White et al. (1986) and Christian & Swank (1997) show that models based on the thermal bremsstrahlung mechanism are unphysical. The emission measures found using this model have to be of order  $\sim 10^{60}$  cm $^{-3}$  and they are too large for the plasma cloud near the NS whose radius is only of order 10 $^6$  cm.

Therefore, the CPL and CompST components combined with a BB were applied to fit the X-ray spectra of 4U 1820–30 (see, e.g., Bloser et al. 2000). The BB temperature  $kT_{\text{BB}}$ , the photon index  $\Gamma$ , and the exponential cutoff energy  $E_C$  are the CPL+BB model parameters. Bloser et al. (2000) also included photoelectric absorption at low energies using the cross section of Morrison & McCamman (1983). White et al. (1986) and Hirano et al. (1987) show that a Gaussian at  $\sim 6.7$  keV is often needed to take into account a blend of  $K_\alpha$  iron lines. Parsignault & Grindlay (1978) applied a power-law fit to the 4U 1820–30 ANS (Astronomische Nederlandse Satelliet) data and found X-ray spectral changes due to intensity variations. These authors found that the photon index  $\Gamma$  changes from 2 at high count rates to 1.4 when the count rate is low. In other words, they found that the spectrum became harder when the luminosity decreased. Stella et al. (1987) used the CPL+BB model to fit the data of the EXOSAT ME instrument in the energy range from 1 to 30 keV. These particular EXOSAT data were obtained during 1984–1985. The source was found at a high-luminosity state ( $6.0 \times 10^{37}$  erg s $^{-1}$ ) and a low-luminosity state ( $2.0 \times 10^{37}$  erg s $^{-1}$ ). The best-fit parameters of these EXOSAT spectra ( $\Gamma$ ,  $E_C$ , and  $kT_{\text{BB}}$ ) are 1.7, 12 keV, and 2 keV, respectively, in the high state and  $\Gamma \sim 2.5$ ,  $E_C > 30$  keV, and  $kT_{\text{BB}} = 2.3$  keV in the low state.

Smale et al. (1994) analyzed the ASCA/GIS data for 4U 1820–30, which was observed in the low state in 1993. They fit the 0.6–11 keV spectrum using the CompST + BB model. The best-fit CompST parameters were around 3.6, 13.5, and 0.76 keV for the plasma temperature, optical, and a BB tem-

perature, respectively. Christian & Swank (1997) reported on the *Einstein* (SSS + MPC) 1978 observation in the 0.5–20 keV energy range. They found that the source was in the high state characterized by a luminosity of  $5.5 \times 10^{37}$  erg s $^{-1}$  and the best-fit parameters of the CompST+BB model were very similar to those obtained using the ASCA data.

Piraino et al. (1999) and Kaaret et al. (1999) analyzed the first observations of 4U 1820–30 extending above  $\sim 30$  keV. For this analysis, they used the observations obtained by the Narrow Field Instruments (NFIs, 0.1–200 keV) of *BeppoSAX* in 1998. The best-fit parameters of the observed spectrum in the 0.3–40 keV energy range are  $kT_{\text{BB}} = 0.47$  keV,  $\Gamma = 0.55$ , and  $E_C = 4.5$  keV for the CPL+BB model, whereas the best-fit parameters of the CompST+BB model are  $kT_{\text{BB}} = 0.46\text{--}0.66$  keV,  $kT_e = 2.83$  keV, and  $\tau = 13.7$ . It is worth noting that the instruments with a response below 1 keV provide low values of  $kT_{\text{BB}}$ . Although the range of luminosities and the best-fit parameters inferred using *BeppoSAX* and the CompST + BB model gave very similar values with respect to those obtained using the other instruments (see above).

The *BeppoSAX* Phoswich Detection System (PDS) could not detect the emission from 4U 1820–30 above 40 keV. Note, BATSE (see Bloser et al. 1996) also failed to find this source in the 20–100 keV range during the first four years of the CGRO. For the first time, a high energy tail above 50 keV has been found by *INTEGRAL* in the hard state of 4U 1820–30 (Tarana et al. 2006), which put this source in the list of X-ray bursters that exhibit high-energy emission.

It is interesting to also note that other atolls can be described by similar spectral models. Lin et al. (2007), hereafter LRH07, pointed out that at the low- $L_X$  end of the soft-state track a weak Comptonization component is needed. LRH07 modified the BPL and COMPTT models, applying their modifications to atolls Aql X-1 and 4U 1608-52. They were interested to find out how much energy is directly visible as a pure thermal radiation and thus one can obtain the remaining fraction for the Comptonized radiation  $f$ . In this sense, this approach is similar to that using the COMPTB model (see Section 3 below). In this way, to account for specific spectra, LRH07 describe the hard state by means of a BB+BPL model and the soft state by means of a three-component model, MCD+BB+CBPL, where CBPL is a broken power law with the high energy cutoff taking into account the Comptonization effect.

In this paper, we show a thorough X-ray spectral-timing analysis of the data for 4U 1820–30 using the *BeppoSAX* and RXTE/PCA/HEXTE available observations that were made during 1998–1999 and 1996–2009. Unlike the past spectral analysis, we adopt a unified model, capable of describing the spectra observed during both the soft and hard states. The full list of observations used in our data analysis is presented in Section 2 and Tables 1 and 2. We describe in detail our spectral model and spectral analysis using this model in Section 3. We interpret X-ray spectral-timing evolution when the source undergoes the spectral state transition in Sections 4–6. We explain our results in detail and come to the final conclusions in Sections 7 and 8.

## 2. DATA SELECTION

We obtained broadband energy spectra of the source using data from three *BeppoSAX* NFIs, namely the Low Energy Concentrator Spectrometer (LECS) with the 0.3–4 keV energy band, the Medium Energy Concentrator Spectrometer (MECS) with the 1.8–10 keV band, and the PDS with the 15–200 keV

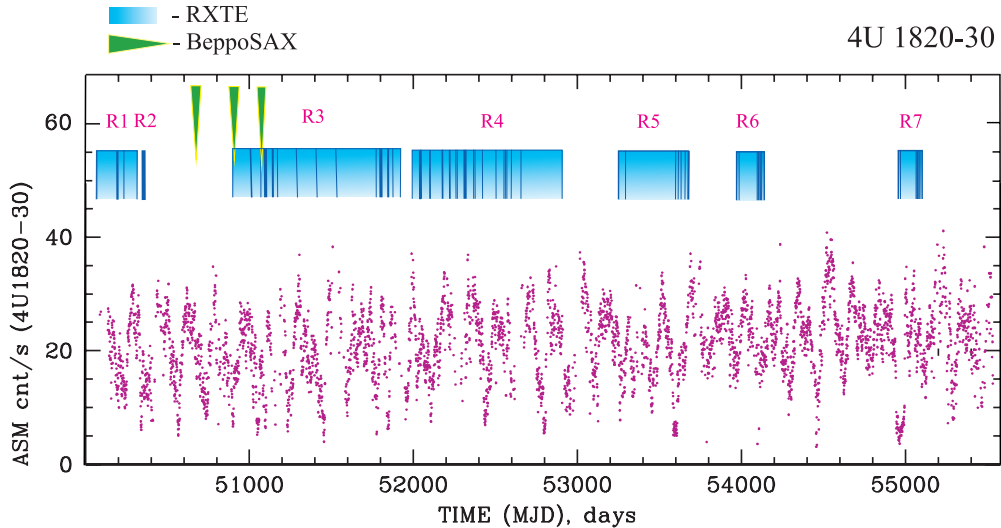


**Figure 1.** Evolution of the ASM/RXTE count rate during the 1996–2009 observations of 4U 1820–30. Blue vertical strips (at top of the panel) indicate the temporal distribution of the RXTE data of pointed observations used in our analysis, while the bright blue rectangles indicate the RXTE data sets listed in Table 2, and the green triangles show BeppoSAX NFI data listed in Table 1.

(A color version of this figure is available in the online journal.)

**Table 1**  
BeppoSAX Observations of 4U 1820–30 Used in the Analysis

Observational ID	Start Time (UT)	End Time (UT)	MJD Interval
20105004	1997 Oct 2 06:45:23	1997 Oct 2 19:09:36	50723.2–50723.8
20537004	1998 Apr 17 04:31:23	1998 Apr 18 02:55:28	50920.1–50921.1 <sup>1</sup>
20537005	1998 Sept 23 12:44:56	1998 Sept 24 15:30:05	51079.5–51080.6 <sup>1</sup>

**Reference.** (1) Kaaret et al. 1999.

**Table 2**  
Groups of RXTE Observations of 4U 1820–30

Number of Set	Dates, MJD	RXTE Proposal ID	Dates UT	Reference
R1	50204–50207	10074	1996 May 1–4	1
	50151, 50235	10076	1996 Mar 9 and Jun 1	1
	50371–50386	10075	1996 Oct 15–30	1, 2, 3, 4
R2	50488–50701	20075	1997 Feb 9–Sep 10	1, 3, 4, 5, 6, 7
	50920–51467	30053, 30057	1998 Apr 4–1999 Oct 16	3
R3	51206–51956	40017, 40019	1999 Jan 28–2003 Jun 4	
	51996–51999	60030	2001 Mar 28–31	
	52355, 52429	40017	2002 Mar 22; 2003 Jun 6	
	52439	70031	2002 Jun 14 13:21:52–14:14:40	
	52482–52808	70030	2002 Jul 23–2003 Jun 18	8
R4	52894	80105	2003 Sep 12 05:41:04–09:36:32	8
	53258–53591	90027	2004 Sep 10–2005 Aug 9	
	53692–53693	91435	2005 Nov 18–19	
R5	53959–54028	91151	2006 Aug 12 and Oct 9	
	53921–54306	92030	2006 Jul 5–2007 Jul 25	
	54126–54129	70030	2007 Jan 26–29	
R7	54947–55002	94090	2009 Apr 26–Jun 20	9
	54947–55116	92030	2009 Sep 8–Oct 12	

**References.** (1) Chou & Grindlay 2001; (2) Smale et al. 1997; (3) Kaaret et al. 1999; (4) Zhang et al. 1998; (5) Bloser et al. 2000; (6) Kuśmirek et al. 2011; (7) Shaposhnikov & Titarchuk 2004; (8) Migliari et al. 2004; (9) Krimm et al. 2009.

band (see Parmar et al. 1997; Boella et al. 1997; Frontera et al. 1997, respectively).

We used the SAXDAS data analysis package for data processing. We renormalized the LECS data based on the MECS

data. We treated relative normalizations of the NFIs as free parameters when we proceeded with model fitting, but we fixed the MECS normalization at 1. Each of these normalizations is controlled if they are in a standard range for a given

**Table 3**  
Best-fit Parameters of Spectral Analysis of *BeppoSAX* Observations of 4U 1820–30 in the 0.3–200 keV Energy Range<sup>a</sup>

Observational ID	MJD (day)	$T_{\text{BB}}$ (keV)	$N_{\text{BB}}^{\text{b}}$	$T_s$ (keV)	$\alpha = \Gamma - 1$	$T_e$ (keV)	$\log(A)$	$N_{\text{COMPTB}}$	$E_{\text{line}}$ , (keV)	$N_{\text{line}}^{\text{b}}$	$\chi^2_{\text{red}}$ (dof)
20105004	50723.28	0.63(3)	2.33(2)	1.35(2)	1.00(4)	3.25(2)	-0.11(5)	3.45(2)	6.7(1)	0.45(2)	1.11(364)
20537004	50920.19	0.58(1)	2.74(3)	1.24(5)	1.01(5)	3.42(2)	-0.10(6)	4.42(6)	6.6(5)	1.38(7)	0.89(364)
20537003	51079.53	0.69(2)	2.68(3)	1.27(4)	0.99(8)	3.37(1)	-0.12(4)	4.65(1)	6.5(2)	0.41(5)	1.2(234)

**Notes.** Parameter errors correspond to a 90% confidence level.

<sup>a</sup> The spectral model is  $wabs * (\text{Blackbody} + \text{CompTB} + \text{Gaussian}) * smedge$ , where  $N_H$  is fixed at a value  $3.00 \times 10^{21} \text{ cm}^{-2}$  (Bloser et al. 2000).

<sup>b</sup> Normalization parameters of Blackbody and CompTB components are in units of  $10^{-2} \times L_{39}/d_{10}^2 \text{ erg s}^{-1} \text{ kpc}^{-2}$ , where  $L_{39}$  is the source luminosity in units of  $10^{39} \text{ erg s}^{-1}$ ,  $d_{10}^2$  is the distance to the source in units of 10 kpc and the Gaussian component is in units of  $10^{-2} \times \text{total photons cm}^{-2} \text{ s}^{-1}$  in line, wherein  $\sigma_{\text{line}}$  of the Gaussian component is fixed at a value 0.8 keV (see comments in the text); smeared edge included at 7.7 keV.

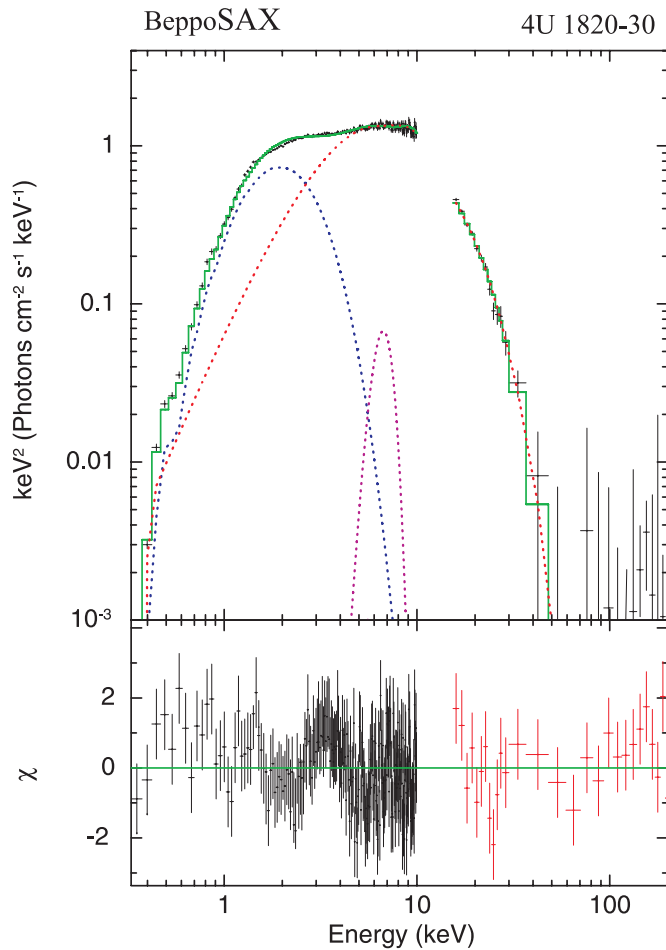


**Figure 2.** Top: the best-fit spectrum of 4U 1820–30 during banana branch events in  $E * F(E)$  units using *BeppoSAX* observation 20105004 carried out on 1997 October 2. The data are presented by crosses and the best-fit spectral model  $wabs * (\text{Blackbody} + \text{CompTB} + \text{Gaussian})$  is shown with a green line. The model components are shown by black, red, and blue lines for Blackbody, CompTB, and Gaussian components, respectively. Bottom panel:  $\Delta\chi^2$  (reduced  $\chi^2 = 1.11$  for 364 dof). The best-fit model parameters are  $\Gamma = 2.00 \pm 0.04$ ,  $kT_e = 3.25 \pm 0.02$  keV, and  $E_{\text{line}} = 6.7 \pm 0.1$  keV (see more details in Table 3).

(A color version of this figure is available in the online journal.)

instrument.<sup>5</sup> Furthermore, we rebinned the spectra to obtain significant data points. The LECS spectra were rebinned using a binning factor that varies with energy (Section 3.1.6 of Cookbook for the *BeppoSAX* NFI spectral analysis), imple-

menting the rebinning template files in GRPPHA of XSPEC.<sup>6</sup> The PDS spectra were rebinned with a linear binning factor of two; we group two bins together leading to the bin width of 1 keV. For all of these spectra, we use a systematic error of 1%. The *BeppoSAX* observations used in our analysis are shown in Table 1.

We also use publicly available *RXTE* data sets (Bradt et al. 1993) that were obtained from 1997 April to 2009 March. In total, they include 92 observations taken at different states of the source. The LHEASOFT/FTOOLS 5.3 software package was applied to process the data. Also for our spectral analysis, we applied PCA *Standard 2* mode data, collected in the 3–20 keV energy range. We also used the most recent release of PCA response calibration (ftool pcarmf v11.1) and the standard dead time correction to the data.

A background subtraction in off-source observations is performed on the data. We use only data from 20 to 150 keV energy in order to avoid the problems related to the HEXTE response and background determination. We apply the GSFC public archive to analyze all available data sets (see <http://heasarc.gsfc.nasa.gov>). We present a full list of observations covering the source evolution during different spectral-state events in Table 2.

We implement an analysis of 13 years of *RXTE* observations of 4U 1820–30 for seven intervals (see blue rectangles in Figure 1 (top)). We fitted the *RXTE* energy spectra using XSPEC astrophysical fitting software. For our data analysis, we have also applied the publicly available 4U 1820–30 data in the energy range from 2 to 10 keV from the All-Sky Monitor (ASM/*RXTE*) for all observation scans.

According to the ASM monitoring system, 4U 1820–30 shows long-term variations with a possible period of  $\sim 176$  days of the 2–10 keV flux (see Figure 1 and Priedhorsky & Terrell 1984; Simon 2003; Wen et al. 2006). The count rate changes in the interval of 5–35 counts  $\text{s}^{-1}$  throughout each cycle (Figure 1). Our *RXTE* spectral studies are directed to investigate: (1) the continuum spectrum, in particular, the hard X-ray tail and its evolution during long-term flux variations, (2) the variation ( $\gtrsim 10$  s) of the best-fit spectral parameters for short- and long-term phases, and (3) the dependence of the spectral index and the electron temperature on the total flux and accretion rate. Data from the PCA and HEXTE detectors as well as *BeppoSAX* detectors have been used to constrain spectral fits, while ASM data provided long-term intensity state monitoring. Results of our long-term study of 4U 1820–30 are presented in detail in the next sections and compared with our previous results for 4U 1728–34 and GX 3+1.

<sup>5</sup> <http://heasarc.nasa.gov/docs/sax/abc/saxabc/saxabc.html>

<sup>6</sup> <http://heasarc.gsfc.nasa.gov/FTP/sax/cal/responses/grouping>

**Table 4**  
Best-fit Parameters of Spectral Analysis of PCA and HEXTE/RXTE Observations of 4U 1820–30 in the 3–200 keV Energy Range<sup>a</sup>

Observational ID	MJD (day)	$\alpha = \Gamma - 1$	$T_e$ (keV)	$\log(A)^b$	$N_{\text{COMPTB}}^c$	$T_s$ (keV)	$N_{\text{Bbody}}^c$	$E_{\text{line}}$ , (keV)	$N_{\text{line}}^c$	$\chi^2_{\text{red}}$ (dof)	$F_1/F_2^d$
10076-01-01-00	50151.937	1.00(2)	2.87(2)	2.00 <sup>b</sup>	7.13(1)	1.30(5)	3.42(1)	6.27(8)	1.1(1)	1.54(78)	6.13/2.24
10074-01-01-00	50204.375	1.0(1)	2.93(4)	2.00 <sup>b</sup>	5.5(2)	1.0(1)	2.31(3)	6.52(6)	0.15(3)	0.92(78)	4.58/1.61
10074-01-01-01	50204.511	0.99(2)	2.91(1)	2.00 <sup>b</sup>	5.3(1)	1.08(2)	2.57(4)	6.5(1)	0.23(3)	0.93(78)	4.52/1.58
10074-01-01-02	50204.785	1.00(2)	2.95(2)	0.92(8)	5.25(9)	1.05(3)	2.48(6)	6.40(4)	0.14(2)	1.06(78)	4.33/1.53
10074-01-02-02	50207.381	1.00(5)	2.84(2)	0.9(1)	7.5(1)	1.06(5)	2.15(4)	6.58(4)	0.23(3)	1.09(78)	5.90/2.06
10074-01-02-00	50207.591	0.99(2)	2.86(1)	2.00 <sup>b</sup>	7.74(2)	1.13(1)	2.46(7)	6.48(3)	0.32(5)	1.58(78)	6.29/2.37
10074-01-02-01	50207.927	0.99(3)	2.89(3)	2.00 <sup>b</sup>	7.42(8)	1.06(4)	2.16(3)	6.38(5)	0.20(2)	0.87(78)	6.05/2.33
10076-01-02-00	50235.532	0.99(2)	2.89(2)	1.09(7)	4.91(1)	1.31(5)	1.96(1)	6.57(4)	0.22(2)	0.74(78)	4.05/1.43
10075-01-01-000	50371.943	1.00(2)	3.02(1)	2.00 <sup>b</sup>	4.0(2)	1.07(2)	2.27(1)	6.49(3)	0.12(1)	1.63(78)	3.47/1.36
10075-01-01-010	50382.566	0.99(2)	3.09(2)	2.00 <sup>b</sup>	3.66(3)	1.30(3)	2.03(2)	6.62(7)	0.14(1)	1.08(78)	3.16/1.30
10075-01-01-020	50384.633	0.96(9)	2.84(1)	2.00 <sup>b</sup>	4.73(1)	1.31(5)	2.18(1)	6.53(4)	0.15(2)	1.24(78)	3.91/1.43
10075-01-01-031	50386.830	0.99(2)	2.89(2)	0.98(4)	5.43(4)	1.31(2)	2.18(2)	6.64(3)	0.23(3)	1.23(78)	4.43/1.58
20075-01-01-00	50488.426	1.01(2)	2.90(2)	2.00 <sup>b</sup>	6.92(3)	1.30(8)	2.65(3)	6.56(2)	0.24(2)	0.74(78)	5.34/1.89
20075-01-02-00	50513.955	0.99(2)	2.85(1)	0.90(5)	7.99(4)	1.32(6)	2.58(5)	6.57(4)	0.29(4)	0.94(78)	6.29/2.19
20075-01-02-01	50514.001	1.00(1)	2.92(1)	2.00 <sup>b</sup>	7.86(3)	1.11(2)	2.60(3)	6.51(3)	0.26(4)	0.94(78)	6.51/2.53
20075-01-03-01	50528.638	0.97(6)	2.92(5)	2.00 <sup>b</sup>	5.05(2)	1.10(5)	2.73(4)	6.44(8)	0.17(5)	1.03(78)	4.27/1.54
20075-01-03-00	50530.705	0.95(1)	2.91(2)	0.65(5)	6.47(7)	1.11(3)	2.55(3)	6.60(3)	0.20(2)	0.94(78)	5.03/1.80
20075-01-04-00	50548.703	0.96(3)	2.95(1)	0.7(1)	5.53(5)	1.23(8)	2.49(2)	6.56(3)	0.18(2)	1.01(78)	3.90/1.44
20075-01-05-00	50570.585	0.99(2)	3.93(2)	0.8(1)	3.22(2)	1.10(2)	2.27(1)	6.90(6)	0.14(3)	1.01(78)	2.49/1.42
20075-01-05-01	50578.549	1.00(2)	2.84(4)	2.00 <sup>b</sup>	6.42(4)	1.12(4)	2.29(2)	6.40(5)	0.38(4)	1.01(78)	5.23/1.86
20075-01-06-00	50595.327	0.99(3)	2.88(2)	1.03(4)	7.96(1)	1.11(6)	2.83(5)	6.54(3)	0.47(3)	1.01(78)	6.46/2.30
20075-01-06-01	50596.432	1.00(2)	2.83(3)	0.96(1)	8.49(1)	1.10(5)	2.73(3)	6.40(6)	0.45(3)	1.01(78)	6.75/2.36
20075-01-07-01	50622.760	1.01(2)	2.86(2)	0.97(4)	8.37(4)	1.11(7)	3.26(7)	6.50(3)	0.61(4)	1.01(78)	6.90/2.38
20075-01-07-00	50622.546	1.00(1)	2.86(2)	0.97(3)	8.31(3)	1.10(5)	3.24(6)	6.48(2)	0.63(4)	1.01(78)	6.86/2.36
20075-01-08-00	50645.216	1.00(2)	2.93(1)	2.00 <sup>b</sup>	7.86(1)	1.10(9)	2.83(2)	6.44(3)	0.30(3)	1.01(78)	6.48/2.56
20075-01-08-01	50645.485	1.00(1)	2.91(1)	2.00 <sup>b</sup>	6.37(4)	1.10(7)	2.73(7)	6.50(4)	0.40(5)	1.01(78)	5.33/1.89
20075-01-09-00	50675.454	0.99(1)	2.87(3)	0.67(2)	7.81(2)	1.12(8)	2.74(5)	6.52(5)	0.46(7)	1.01(78)	5.97/2.04
20075-01-10-00	50701.149	1.00(1)	2.92(2)	2.00 <sup>b</sup>	4.90(3)	1.11(5)	2.91(1)	6.37(3)	0.41(4)	1.09(78)	4.35/1.56
20075-01-10-01	50701.251	1.00(2)	2.91(1)	2.00 <sup>b</sup>	5.17(3)	1.10(6)	2.90(5)	6.37(3)	0.41(4)	1.09(78)	4.56/1.63
30057-01-01-01	50907.412	1.02(5)	3.00(2)	0.70(3)	4.51(1)	1.12(5)	2.40(1)	6.5(1)	0.31(1)	1.76(78)	3.63/1.32
30057-01-01-00	50908.660	1.00(1)	2.83(1)	1.02(1)	6.18(2)	1.11(2)	2.35(7)	6.41(9)	0.37(2)	1.20(78)	4.95/1.74
30057-01-01-02	50909.662	1.01(3)	2.95(1)	0.72(2)	5.06(3)	1.10(4)	2.58(5)	6.51(8)	0.29(2)	1.12(78)	4.05/1.45
30057-01-01-03	50910.589	1.00(1)	2.94(2)	0.66(2)	5.43(1)	1.12(5)	2.53(6)	6.6(1)	0.33(2)	0.79(78)	4.29/1.52
30057-01-01-04	50910.790	0.99(2)	2.87(2)	0.77(2)	6.20(3)	1.12(5)	2.64(7)	6.5(1)	0.32(1)	0.79(78)	4.74/1.68
30053-03-01-000	50920.197	0.99(4)	2.93(2)	2.00 <sup>b</sup>	4.74(5)	1.10(2)	2.62(4)	6.54(2)	0.34(2)	0.57(78)	4.07/1.45
30053-03-02-00	51079.552	1.00(3)	2.91(1)	0.75(1)	6.42(1)	1.11(1)	2.84(2)	6.52(3)	0.36(3)	1.17(78)	5.06/1.83
30053-03-02-01	51079.719	1.00(2)	2.89(4)	0.73(1)	6.45(3)	1.10(5)	2.77(2)	6.51(4)	0.34(3)	1.19(78)	5.05/1.80
30053-03-02-04	51079.812	0.99(1)	2.86(2)	0.99(5)	5.97(1)	1.12(6)	2.84(2)	6.45(9)	0.77(1)	1.22(78)	4.97/1.76
30053-03-02-05	51079.879	0.9(1)	2.86(5)	0.41(3)	5.91(2)	1.11(4)	2.86(2)	6.65(6)	0.15(3)	0.90(78)	4.37/1.54
30053-03-02-02	51080.229	0.99(4)	2.99(1)	0.74(1)	4.59(1)	1.10(5)	2.63(1)	6.51(4)	0.19(2)	1.13(78)	3.73/1.35
30053-03-02-03	51080.413	1.00(3)	2.93(3)	2.00 <sup>b</sup>	4.09(3)	1.11(2)	2.58(3)	6.42(5)	0.29(1)	1.17(78)	3.50/1.28
30057-01-02-00	51320.532	0.98(3)	2.96(3)	0.85(1)	5.28(4)	1.12(3)	3.43(7)	6.51(6)	0.31(3)	0.86(78)	4.71/1.59
30057-01-02-01	51321.713	1.00(1)	2.99(1)	0.72(3)	6.02(4)	1.10(4)	3.36(1)	6.5(1)	0.47(5)	0.84(78)	4.89/1.76
30057-01-02-02	51323.729	1.01(3)	2.93(1)	2.00 <sup>b</sup>	4.92(3)	1.11(5)	3.47(1)	6.51(4)	0.33(1)	0.82(78)	4.20/1.53
30057-01-02-03	51324.378	1.00(1)	2.95(2)	0.92(3)	5.12(3)	1.12(2)	3.29(6)	6.42(6)	0.32(2)	1.24(78)	4.28/1.55
30057-01-02-05	51324.511	1.02(3)	2.94(1)	0.91(4)	5.03(2)	1.12(3)	3.33(5)	6.51(9)	0.33(1)	0.97(78)	4.23/1.52
30057-01-03-01	51410.501	1.00(3)	2.91(2)	0.84(3)	4.93(3)	1.13(2)	3.01(6)	6.57(8)	0.32(2)	0.98(78)	4.08/1.43
30057-01-03-02	51411.499	0.99(2)	2.94(1)	0.96(4)	4.63(4)	1.12(5)	3.01(1)	6.54(9)	0.35(2)	0.98(78)	3.89/1.41
30057-01-03-000	51412.315	1.02(4)	2.87(4)	0.91(4)	5.82(3)	1.12(4)	2.94(1)	6.51(5)	0.46(3)	1.50(78)	4.71/1.68
30057-01-04-12	51418.427	1.00(2)	2.83(3)	2.00 <sup>b</sup>	3.84(7)	1.15(5)	2.83(7)	6.49(8)	0.30(4)	0.76(78)	3.42/1.21
30057-01-04-00	51418.557	0.98(3)	2.87(1)	2.00 <sup>b</sup>	3.89(3)	1.14(2)	2.93(6)	6.48(9)	0.27(1)	1.10(78)	3.38/1.21
30057-01-04-01	51419.289	1.00(2)	2.93(1)	2.00 <sup>b</sup>	3.54(1)	1.11(3)	2.48(2)	6.5(1)	0.29(2)	1.50(78)	3.06/1.17
30057-01-04-02	51419.427	1.00(1)	2.95(2)	2.00 <sup>b</sup>	3.60(2)	1.12(2)	2.43(5)	6.43(4)	0.29(1)	0.86(78)	3.09/1.18
30057-01-04-03	51424.416	1.02(3)	2.91(1)	2.00 <sup>b</sup>	3.77(2)	1.12(2)	2.49(5)	6.51(6)	0.27(2)	0.78(78)	3.19/1.17
30057-01-04-04	51424.483	0.99(3)	2.93(1)	2.00 <sup>b</sup>	3.75(3)	1.16(3)	2.50(5)	6.56(5)	0.28(3)	0.85(78)	3.18/1.18
30057-01-04-05	51432.379	1.00(1)	2.92(2)	0.88(4)	3.31(2)	1.11(4)	2.19(4)	6.51(1)	0.31(4)	0.75(78)	2.78/0.98
30057-01-04-06	51425.348	0.98(3)	2.93(2)	0.86(3)	4.53(3)	1.11(2)	2.39(5)	6.52(9)	0.36(1)	1.08(78)	3.68/1.34
30057-01-04-07G	51428.354	1.03(3)	2.89(1)	2.00 <sup>b</sup>	2.91(2)	1.12(1)	1.87(3)	6.58(5)	0.24(4)	1.08(78)	2.47/0.91
30057-01-04-08G	51430.007	1.00(1)	2.89(1)	2.00 <sup>b</sup>	2.91(2)	1.12(2)	1.87(3)	6.51(2)	0.24(5)	1.04(78)	2.47/0.91
30057-01-05-00	51435.001	0.99(1)	2.89(2)	0.61(4)	4.86(5)	1.14(5)	2.93(1)	6.56(3)	0.41(1)	1.18(78)	3.85/1.29
30057-01-04-09	51436.225	0.98(3)	2.93(1)	0.60(4)	4.77(4)	1.13(4)	2.81(3)	6.51(6)	0.35(1)	0.98(78)	3.75/1.29
30057-01-06-02	51466.231	1.00(2)	2.93(1)	1.02(7)	5.55(9)	1.12(2)	3.65(8)	6.47(3)	0.57(8)	1.46(78)	4.82/1.70
30057-01-06-03	51466.440	1.00(1)	2.91(1)	1.02(8)	5.83(9)	1.11(2)	3.71(9)	6.50(7)	0.53(7)	0.79(78)	4.99/1.72
30057-01-06-00	51466.499	0.97(3)	2.93(2)	0.97(7)	5.62(6)	1.11(5)	3.67(5)	6.55(6)	0.60(8)	1.18(78)	4.86/1.71
30057-01-06-04	51466.965	1.01(3)	2.91(1)	0.96(9)	6.18(8)	1.10(3)	3.95(9)	6.51(4)	0.75(9)	1.12(78)	5.35/1.85

**Table 4**  
(Continued)

Observational ID	MJD (day)	$\alpha = \Gamma - 1$	$T_e$ (keV)	$\log(A)^b$	$N_{\text{COMPTB}}^c$	$T_s$ (keV)	$N_{\text{Body}}^c$	$E_{\text{line}}$ , (keV)	$N_{\text{line}}^c$	$\chi^2_{\text{red}}$ (dof)	$F_1/F_2^d$
30057-01-06-01	51467.035	1.00(1)	2.92(2)	0.84(8)	5.96(7)	1.12(3)	3.84(6)	6.52(6)	0.69(4)	0.69(78)	5.09/1.74
30057-01-06-05	51467.098	0.99(2)	2.96(2)	1.00(9)	5.54(1)	1.12(2)	3.89(9)	6.52(8)	0.54(8)	0.72(78)	4.83/1.72
40017-01-01-00	51206.852	1.01(3)	2.88(9)	1.08(3)	7.37(9)	1.20(4)	3.08(8)	6.50(4)	0.50(7)	0.81(78)	6.10/2.24
40017-01-01-02	51206.924	0.99(3)	2.93(5)	0.91(3)	7.40(8)	1.21(2)	2.98(9)	6.51(5)	0.90(9)	1.00(78)	6.01/2.22
40017-01-01-01	51207.002	1.00(2)	2.91(1)	2.00 <sup>b</sup>	7.03(9)	1.13(3)	3.03(8)	6.52(7)	0.91(9)	0.90(78)	5.91/2.18
40017-01-01-03	51207.128	1.00(2)	2.94(2)	2.00 <sup>b</sup>	6.96(9)	1.12(2)	3.06(7)	6.57(3)	0.36(4)	0.88(78)	5.83/2.15
40017-01-02-00	51222.642	0.98(3)	3.00(1)	2.00 <sup>b</sup>	4.97(6)	1.14(5)	3.47(6)	6.54(7)	0.90(7)	1.30(78)	4.58/1.72
40017-01-03-00	51238.040	1.06(4)	2.90(3)	2.00 <sup>b</sup>	3.23(7)	1.13(2)	2.31(4)	5.59(3)	0.16(5)	1.31(78)	2.82/1.05
40017-01-03-01	51238.242	1.02(3)	2.88(2)	2.00 <sup>b</sup>	3.14(8)	1.12(4)	2.30(4)	6.15(6)	0.12(6)	1.21(78)	2.71/1.02
40017-01-04-00	51253.697	1.00(1)	2.97(1)	2.00 <sup>b</sup>	4.62(3)	1.13(5)	2.60(5)	6.21(5)	0.24(7)	0.86(78)	3.98/1.49
40017-01-05-00	51268.750	1.00(2)	2.91(3)	2.00 <sup>b</sup>	7.67(9)	1.12(2)	3.27(1)	6.18(7)	0.44(8)	1.09(78)	6.41/2.53
40017-01-06-00	51283.608	1.07(4)	2.88(2)	0.79(5)	9.98(6)	1.15(2)	3.93(3)	6.51(1)	0.59(6)	1.40(78)	7.89/2.81
40017-01-06-01	51283.768	1.04(3)	2.93(1)	2.00 <sup>b</sup>	10.46(7)	1.13(1)	3.97(4)	6.41(1)	0.62(7)	1.24(78)	8.39/3.22
40017-01-05-01	51296.888	1.01(3)	2.91(2)	0.78(4)	7.71(8)	1.12(5)	2.99(2)	6.21(6)	0.46(5)	1.03(78)	6.02/2.21
40017-01-07-01	51300.010	1.00(2)	2.89(2)	0.92(6)	11.61(8)	1.12(2)	5.07(2)	6.41(9)	2.19(6)	1.04(78)	9.52/3.39
40017-01-07-00	51300.067	1.00(1)	2.94(1)	0.70(8)	10.35(9)	1.14(5)	4.58(3)	6.27(5)	1.72(8)	1.51(78)	8.31/2.93
40017-01-08-00	51313.655	1.01(3)	2.95(2)	0.87(3)	6.93(9)	1.13(2)	3.62(1)	6.49(7)	1.20(1)	1.04(78)	5.79/2.09
40017-01-09-00	51330.505	1.00(1)	2.90(1)	0.79(2)	8.12(5)	1.14(3)	3.65(1)	6.41(4)	1.21(2)	1.03(78)	6.51/2.32
40017-01-10-00	51343.836	1.00(2)	2.90(2)	1.00(3)	7.79(8)	1.11(2)	3.60(1)	6.43(6)	1.52(7)	1.06(78)	6.62/2.42
40017-01-10-01	51343.901	0.99(7)	2.91(2)	0.91(0)	7.37(9)	1.12(3)	3.76(9)	6.51(3)	0.46(4)	1.50(78)	6.13/2.17
40017-01-10-02	51343.968	0.99(3)	2.87(1)	1.07(9)	7.88(6)	1.14(1)	3.68(2)	6.59(7)	1.29(5)	1.24(78)	6.60/2.36
40017-01-11-01	51355.422	1.00(1)	2.95(2)	0.95(1)	6.13(6)	1.15(5)	3.06(1)	6.51(1)	0.33(5)	0.88(78)	5.13/1.90
40017-01-11-02	51355.489	1.00(2)	2.93(2)	0.97(3)	6.87(8)	1.12(2)	2.93(2)	6.63(7)	0.35(4)	1.09(78)	5.64/2.11
40017-01-11-00	51355.562	0.99(2)	2.94(1)	0.92(3)	6.56(7)	1.13(1)	2.98(1)	6.53(6)	0.37(7)	1.00(78)	5.37/1.99
40017-01-12-00	51389.381	0.99(3)	2.94(1)	2.00 <sup>b</sup>	7.80(6)	1.13(2)	3.29(1)	6.24(3)	0.63(2)	1.10(78)	6.48/2.63
40017-01-11-03	51495.992	0.98(3)	2.95(2)	0.74(2)	7.31(5)	1.12(4)	4.58(3)	6.38(6)	0.56(3)	1.00(78)	6.41/2.19
40017-01-12-01	51496.185	1.00(3)	2.99(1)	0.72(2)	7.25(6)	1.14(5)	4.42(2)	6.21(8)	0.59(1)	1.47(78)	6.29/2.20
40017-01-13-00	51400.444	1.00(2)	2.94(1)	0.79(4)	7.59(4)	1.13(2)	3.13(1)	6.58(2)	0.41(2)	1.20(78)	6.00/2.23
40017-01-14-00	51407.503	1.02(3)	2.92(2)	0.82(3)	5.68(4)	1.12(5)	2.85(2)	6.5(2)	0.34(2)	1.17(78)	4.71/1.71
40017-01-15-00	51417.295	1.01(2)	3.00(1)	0.97(2)	4.69(3)	1.14(3)	2.69(2)	6.4(1)	0.27(4)	1.39(78)	3.92/1.47
40019-02-01-00	51421.302	1.00(1)	2.97(2)	2.00 <sup>b</sup>	3.82(8)	1.12(2)	2.19(1)	6.57(1)	0.14(5)	1.35(78)	3.31/1.27
40019-02-01-03	51421.635	0.98(4)	3.01(1)	2.00 <sup>b</sup>	3.77(4)	1.11(2)	2.19(1)	6.61(5)	0.19(5)	0.86(78)	3.29/1.29
40019-02-01-04	51421.707	1.00(2)	2.99(1)	2.00 <sup>b</sup>	6.84(3)	1.11(3)	2.09(1)	6.84(3)	0.12(3)	1.28(78)	3.23/1.26
40019-02-01-10	51421.777	1.01(3)	2.97(3)	2.00 <sup>b</sup>	3.87(4)	1.12(4)	2.40(3)	6.75(2)	0.19(1)	1.15(78)	3.39/1.29
40019-02-01-11	51421.846	1.00(2)	2.97(2)	2.00 <sup>b</sup>	3.85(3)	1.13(5)	2.37(1)	6.53(4)	0.13(4)	0.73(78)	3.37/1.28
40019-02-01-01	51421.952	0.98(3)	3.00(2)	2.00 <sup>b</sup>	3.56(3)	1.12(2)	2.20(2)	6.67(3)	0.13(4)	0.86(78)	3.12/1.21
40019-02-01-02G	51422.083	0.99(3)	3.10(3)	2.00 <sup>b</sup>	3.51(4)	1.12(3)	1.96(1)	7.36(6)	0.62(3)	0.79(78)	3.03/1.26
40019-02-01-05G	51422.257	1.01(3)	2.97(2)	2.00 <sup>b</sup>	3.89(3)	1.13(2)	2.33(3)	6.51(4)	0.19(4)	0.91(78)	3.40/1.29
40019-02-01-06	51422.561	1.01(3)	2.98(2)	2.00 <sup>b</sup>	3.72(2)	1.11(5)	2.35(1)	6.51(6)	0.15(3)	0.84(78)	3.27/1.24
40019-02-01-07	51422.634	0.97(6)	2.97(1)	2.00 <sup>b</sup>	3.73(4)	1.12(2)	2.30(1)	6.59(8)	0.14(2)	0.89(78)	3.26/1.24
40019-02-01-09	51422.706	1.00(1)	2.92(1)	2.00 <sup>b</sup>	3.72(3)	1.12(3)	2.34(1)	6.51(3)	0.16(3)	1.34(78)	3.49/1.29
40017-01-16-00G	51429.075	1.04(5)	2.95(1)	2.00 <sup>b</sup>	3.19(2)	1.12(5)	1.96(1)	6.62(5)	0.43(6)	1.28(78)	1.03/1.47
40017-01-17-00	51440.060	0.98(3)	2.97(2)	0.58(9)	4.85(3)	1.14(4)	2.52(2)	6.70(9)	0.69(2)	1.02(78)	3.81/1.35
40017-01-17-01	51440.218	1.00(1)	2.89(2)	0.65(8)	5.22(3)	1.12(3)	2.53(1)	6.52(8)	0.89(1)	1.28(78)	4.13/1.42
40017-01-18-00	51464.368	0.99(3)	2.97(1)	2.00 <sup>b</sup>	5.47(9)	1.13(2)	3.54(2)	6.18(7)	1.08(3)	1.28(78)	4.84/1.79
40017-01-19-00	51480.115	0.97(3)	2.90(1)	0.91(3)	10.98(7)	1.13(3)	4.03(1)	6.46(9)	2.15(4)	0.96(78)	8.79/3.25
40017-01-20-00	51495.667	1.00(1)	2.92(2)	2.00 <sup>b</sup>	7.13(8)	1.14(5)	4.66(2)	6.23(6)	1.93(8)	0.89(78)	8.67/2.22
40017-01-19-01	51496.326	1.00(2)	3.06(2)	0.67(2)	6.97(4)	1.12(3)	4.22(3)	6.85(5)	1.34(5)	0.57(78)	6.02/2.21
40017-01-19-02	51496.395	1.01(3)	2.92(1)	1.06(9)	7.05(5)	1.12(2)	4.47(1)	6.34(7)	1.84(7)	0.98(78)	6.38/2.18
40017-01-20-01	51496.666	0.98(3)	2.98(2)	0.65(9)	8.16(5)	1.14(5)	4.32(1)	6.50(8)	1.55(6)	0.91(78)	6.73/2.34
40017-01-21-00	51941.015	1.00(1)	2.99(4)	0.97(4)	4.05(7)	1.13(4)	1.93(2)	6.22(9)	0.67(9)	0.89(78)	3.43/1.32
40017-01-21-01	51941.240	1.00(3)	3.00(1)	0.80(4)	4.24(3)	1.12(3)	1.77(1)	6.63(4)	0.65(4)	1.04(78)	3.35/1.04
40017-01-21-02	51941.303	0.99(2)	2.96(4)	1.09(5)	3.94(8)	1.11(2)	1.77(1)	6.34(6)	0.64(3)	0.82(78)	3.22/1.00
40017-01-22-00	51955.872	0.99(3)	3.03(1)	0.93(4)	4.73(3)	1.12(1)	2.38(2)	6.32(9)	0.68(6)	1.07(78)	3.94/1.55
40017-01-22-01	51956.009	1.00(2)	3.02(1)	0.96(4)	4.40(3)	1.15(5)	2.26(2)	6.09(5)	0.92(4)	1.11(78)	3.77/1.49
60030-01-01-00	51996.856	1.00(3)	2.97(1)	0.89(4)	10.20(8)	1.12(4)	3.68(3)	6.32(2)	0.56(5)	1.26(78)	8.17/3.03
60030-01-01-01G	51997.785	1.01(2)	2.96(2)	2.00 <sup>b</sup>	13.5(1)	1.14(5)	3.19(2)	6.14(5)	0.74(6)	1.40(78)	10.84/4.49
60030-01-01-02G	51997.851	0.99(3)	2.88(1)	2.00 <sup>b</sup>	12.54(9)	1.12(3)	4.04(5)	6.36(3)	0.78(8)	0.95(78)	10.07/3.71
60030-01-01-03	51997.918	1.00(2)	2.92(1)	2.00 <sup>b</sup>	13.5(1)	1.13(5)	3.05(2)	6.16(4)	0.69(2)	1.26(78)	10.71/4.29
60030-01-02-00	51998.911	0.99(3)	2.94(2)	2.00 <sup>b</sup>	11.72(9)	1.11(2)	3.26(3)	6.38(5)	0.64(3)	1.49(78)	9.29/3.58
60030-01-02-01	51999.642	1.02(2)	2.94(1)	0.92(3)	11.62(8)	1.11(1)	3.45(2)	6.54(3)	0.69(4)	1.17(78)	9.19/3.41
60030-01-02-02	51999.707	1.01(3)	2.94(1)	0.84(4)	11.31(8)	1.12(3)	3.43(2)	6.54(7)	0.62(3)	0.77(78)	8.90/3.25
40017-01-23-00	52355.020	1.00(1)	2.92(2)	0.98(2)	9.48(7)	1.13(5)	4.37(4)	6.31(8)	2.13(3)	1.21(78)	8.21/3.26
40017-01-23-01	52355.883	1.01(3)	2.91(1)	2.00 <sup>b</sup>	10.06(6)	1.53(6)	4.90(1)	6.46(7)	2.14(5)	1.31(78)	11.91/3.55
40017-01-24-00	52429.708	1.01(3)	9.94(9)	0.13(5)	2.32(2)	1.69(3)	1.16(2)	6.80(8)	0.50(1)	1.00(78)	1.50/1.62

**Table 4**  
(Continued)

Observational ID	MJD (day)	$\alpha = \Gamma - 1$	$T_e$ (keV)	$\log(A)^b$	$N_{\text{COMPTB}}^c$	$T_s$ (keV)	$N_{\text{body}}^c$	$E_{\text{line}}$ , (keV)	$N_{\text{line}}^c$	$\chi^2_{\text{red}}$ (dof)	$F_1/F_2^d$
70030-03-02-00	52478.468	1.02(5)	2.92(3)	2.00 <sup>b</sup>	6.59(4)	1.12(4)	2.81(1)	6.27(5)	0.52(6)	1.25(78)	5.52/2.09
70030-03-02-000	52478.137	1.01(3)	2.93(1)	2.00 <sup>b</sup>	6.34(6)	1.14(5)	2.75(1)	6.22(3)	0.43(4)	0.82(78)	5.20/2.02
70030-03-02-01	52479.406	1.01(2)	3.00(2)	2.00 <sup>b</sup>	6.00(5)	1.13(4)	3.09(3)	6.11(3)	0.51(2)	1.13(78)	4.83/1.85
70030-03-02-020	52480.254	1.01(3)	2.94(1)	2.00 <sup>b</sup>	7.48(6)	1.11(2)	2.76(1)	6.18(4)	0.34(3)	1.46(78)	6.18/2.46
70030-03-02-03G	52480.067	0.99(3)	2.94(1)	2.00 <sup>b</sup>	6.47(4)	1.12(3)	2.39(3)	6.17(5)	0.29(2)	1.25(78)	5.35/2.13
70030-03-02-03G	52480.067	1.00(1)	2.94(1)	2.00 <sup>b</sup>	6.47(6)	1.11(2)	2.39(2)	6.18(3)	0.29(3)	1.21(78)	5.35/2.13
70030-03-01-01G	52480.182	0.99(4)	2.93(1)	2.00 <sup>b</sup>	6.63(6)	1.11(4)	2.96(1)	6.25(4)	0.52(4)	1.30(78)	5.56/2.09
70030-03-01-00G	52482.158	1.01(3)	2.90(3)	2.00 <sup>b</sup>	7.81(7)	1.14(5)	3.08(1)	6.14(8)	0.65(2)	1.18(78)	6.52/2.50
70030-03-01-02	52484.157	1.00(1)	2.89(1)	2.00 <sup>b</sup>	8.15(8)	1.13(4)	3.07(2)	6.31(3)	0.54(6)	1.51(78)	6.67/2.47
70030-03-01-03	52487.171	1.00(3)	2.93(4)	2.00 <sup>b</sup>	8.33(6)	1.15(6)	3.08(2)	6.17(2)	0.66(4)	0.86(78)	6.88/2.66
70030-03-03-00	52489.217	1.00(2)	2.90(2)	2.00 <sup>b</sup>	8.30(7)	1.13(2)	3.02(3)	6.13(5)	0.73(3)	0.77(78)	6.87/2.64
70030-03-04-00	52801.149	0.99(3)	5.56(5)	2.00 <sup>b</sup>	2.14(3)	1.12(1)	0.63(1)	6.64(2)	0.19(2)	0.74(78)	1.63/1.46
70030-03-04-01	52802.070	1.00(2)	5.79(3)	0.89(4)	2.35(2)	1.12(2)	0.95(1)	6.65(3)	0.09(1)	1.04(78)	1.63/1.49
70030-03-05-00	52804.043	1.02(3)	5.75(4)	0.90(2)	2.55(1)	1.11(2)	1.40(2)	6.65(2)	0.04(2)	1.19(78)	1.76/1.61
70030-03-05-01	52805.819	1.01(2)	5.34(4)	2.00 <sup>b</sup>	2.99(6)	1.11(1)	1.28(1)	6.57(1)	0.14(3)	1.17(78)	2.11/1.84
70030-03-05-02	52806.937	1.01(3)	4.17(3)	2.00 <sup>b</sup>	3.17(3)	1.12(3)	2.04(2)	5.64(4)	0.53(1)	1.20(78)	2.56/1.68
70030-03-05-03	52808.057	1.03(4)	3.05(2)	2.00 <sup>b</sup>	4.61(2)	1.14(5)	3.01(3)	6.08(7)	0.36(5)	1.44(78)	4.04/1.64
70030-03-05-04	52808.978	1.01(2)	3.06(4)	2.00 <sup>b</sup>	4.61(1)	1.13(4)	2.88(2)	6.40(4)	0.22(4)	1.02(78)	4.04/1.66
70030-03-07-03	54126.393	1.00(2)	3.00(1)	2.00 <sup>b</sup>	4.43(3)	1.15(7)	3.34(2)	6.17(2)	0.65(4)	1.33(78)	4.02/1.53
70030-03-07-01	54127.244	1.00(1)	2.94(1)	2.00 <sup>b</sup>	5.99(1)	1.11(2)	3.56(6)	6.04(1)	1.14(7)	1.22(78)	5.15/1.94
70030-03-07-00	54128.226	1.02(3)	3.00(5)	2.00 <sup>b</sup>	6.78(4)	1.12(1)	3.28(3)	6.30(3)	0.59(1)	0.75(78)	5.66/2.35
70030-03-07-020	54129.013	1.01(2)	2.96(2)	2.00 <sup>b</sup>	5.63(2)	1.12(3)	3.50(2)	6.04(2)	1.13(6)	0.85(78)	5.15/1.94
70031-05-01-00	52439.556	1.01(3)	6.87(2)	0.26(2)	2.77(1)	1.72(2)	2.25(2)	6.14(3)	1.67(7)	1.26(78)	4.02/1.50
80105-07-01-00	52894.237	1.00(1)	3.22(4)	0.19(3)	6.46(9)	1.66(3)	2.25(2)	6.16(2)	1.86(5)	1.12(78)	5.08/1.95
90027-01-01-00	53258.915	1.00(2)	3.11(2)	0.68(3)	3.54(4)	1.40(3)	2.67(2)	6.40(1)	0.02(2)	0.75(78)	2.89/1.19
90027-01-01-01	53259.704	1.00(3)	3.20(3)	0.52(4)	3.41(3)	1.41(2)	2.01(1)	6.41(3)	0.01(1)	1.28(78)	2.59/1.09
90027-01-01-03	53261.935	0.96(4)	3.12(3)	0.33(4)	5.81(6)	1.45(4)	2.67(4)	6.46(2)	0.02(1)	1.11(78)	4.23/1.63
90027-01-01-04	53262.921	1.01(3)	3.22(2)	0.34(3)	5.21(5)	1.39(3)	2.93(2)	6.42(6)	0.06(2)	0.91(78)	4.23/1.53
90027-01-01-05	53263.249	1.00(2)	3.17(2)	0.27(4)	6.12(6)	1.40(5)	2.74(2)	6.49(1)	0.01(1)	1.36(78)	4.43/1.69
90027-01-01-06	53264.495	0.99(3)	3.16(2)	0.32(3)	6.33(5)	1.42(4)	2.85(3)	6.42(5)	0.02(2)	1.15(78)	4.59/1.79
90027-01-02-00	53265.745	1.00(1)	3.12(2)	0.40(3)	7.15(6)	1.46(3)	2.93(2)	6.43(7)	0.03(2)	1.04(78)	5.14/2.08
90027-01-02-01	53266.336	0.99(3)	3.10(1)	0.37(5)	6.43(6)	1.38(2)	2.76(3)	6.42(1)	0.01(1)	1.12(78)	4.65/1.83
90027-01-02-07	53266.727	0.99(3)	3.12(2)	0.40(6)	7.15(7)	1.41(4)	2.93(6)	6.40(3)	0.01(1)	0.87(78)	5.14/2.09
90027-01-02-08	53267.587	1.00(1)	3.08(2)	0.39(4)	6.38(6)	1.43(3)	2.68(8)	6.54(2)	0.03(1)	1.08(78)	4.60/1.82
90027-01-02-03	53268.372	1.01(2)	3.09(1)	0.38(4)	5.65(5)	1.40(1)	2.47(2)	6.41(3)	0.01(1)	1.04(78)	4.09/1.61
90027-01-02-04	53269.289	1.00(1)	3.17(2)	0.35(3)	4.97(4)	1.40(2)	2.47(2)	6.40(4)	0.02(3)	1.29(78)	3.66/1.45
90027-01-02-05	53270.860	0.98(5)	3.15(3)	0.32(1)	6.03(5)	1.42(3)	2.47(8)	6.40(3)	0.03(2)	0.89(78)	4.33/1.71
90027-01-02-06	53271.594	1.00(2)	3.12(2)	0.59(3)	6.13(6)	1.37(2)	2.65(8)	6.44(1)	0.02(1)	0.85(78)	4.46/1.95
90027-01-03-07	53272.498	1.00(2)	3.13(2)	0.32(4)	5.85(6)	1.39(3)	2.61(6)	6.69(5)	0.01(1)	1.04(78)	4.24/1.64
90027-01-03-08	53272.697	0.98(4)	3.08(3)	0.55(4)	5.98(4)	1.41(2)	2.54(8)	6.40(3)	0.02(2)	1.24(78)	4.34/1.84
90027-01-03-00	53273.491	1.01(2)	3.14(4)	0.46(3)	5.70(6)	1.40(1)	2.45(7)	6.69(1)	0.02(1)	0.93(78)	4.14/1.73
90027-01-03-09	53273.561	1.02(3)	3.09(2)	0.41(3)	5.58(5)	1.45(2)	2.32(6)	6.42(4)	0.01(1)	1.17(78)	4.03/1.62
90027-01-03-02	53274.206	1.00(2)	3.16(1)	0.34(6)	4.62(6)	1.42(2)	2.35(4)	6.40(4)	0.01(1)	1.05(78)	3.41/1.33
90027-01-03-01	53274.486	1.01(3)	3.24(2)	0.41(2)	3.71(4)	1.41(1)	2.06(8)	6.41(1)	0.02(1)	1.26(78)	2.78/1.15
90027-01-03-10	53274.759	1.04(4)	3.12(4)	0.51(3)	3.40(3)	1.41(2)	2.23(7)	6.57(8)	0.01(1)	1.08(78)	2.65/1.05
90027-01-03-11	53274.796	1.00(2)	3.12(3)	0.49(2)	3.39(3)	1.44(1)	2.06(2)	6.40(2)	0.02(2)	0.96(78)	2.59/1.04
90027-01-03-03	53275.520	0.99(3)	3.09(2)	0.56(4)	3.42(3)	1.43(2)	2.10(8)	6.43(1)	0.03(2)	1.13(78)	2.62/1.06
90027-01-03-04	53276.113	0.96(5)	3.21(3)	0.50(2)	3.68(6)	1.42(2)	2.25(4)	6.40(3)	0.01(1)	1.07(78)	2.82/1.17
90027-01-03-05	53277.419	1.00(1)	4.03(4)	0.53(3)	3.12(4)	1.40(3)	1.59(5)	6.41(6)	0.02(1)	1.10(78)	2.32/1.35
90027-01-03-06	53278.404	1.01(3)	3.35(3)	0.54(5)	3.64(5)	1.41(2)	2.15(8)	6.42(1)	0.01(1)	1.12(78)	2.77/1.26
90027-01-04-00	53279.267	1.01(2)	3.24(2)	0.30(4)	5.59(6)	1.40(2)	2.76(3)	6.43(4)	0.02(1)	0.97(78)	4.10/1.63
90027-01-04-05	53280.437	1.01(3)	3.09(4)	0.44(3)	4.1(1)	1.64(5)	2.68(4)	6.40(1)	0.09(5)	1.26(78)	3.25/1.31
90027-01-04-01	53281.354	1.02(3)	3.21(2)	0.42(2)	4.53(4)	1.41(2)	2.77(3)	6.40(1)	0.01(1)	0.99(78)	3.45/1.39
90027-01-04-03	53282.272	0.99(3)	3.27(2)	0.32(2)	4.91(6)	1.40(3)	2.73(5)	6.41(4)	0.02(2)	1.06(78)	3.67/1.47
90027-01-04-04	53283.127	1.00(2)	3.13(2)	0.27(1)	5.82(7)	1.42(2)	2.63(2)	6.43(7)	0.01(1)	0.98(78)	4.22/1.58
90027-01-04-02	53283.978	1.00(1)	3.16(1)	0.32(3)	6.08(5)	1.41(2)	2.72(4)	6.46(3)	0.03(1)	0.98(78)	4.41/1.74
90027-01-05-00	53286.080	0.99(4)	3.06(2)	0.9(1)	4.1(1)	1.25(3)	2.42(2)	6.24(5)	0.08(3)	1.16(78)	3.36/1.33
90027-01-06-00	53591.287	1.00(3)	15.06(7)	0.2(1)	2.72(5)	1.65(4)	1.34(1)	6.58(4)	1.43(4)	1.04(78)	1.55/2.09
91435-01-01-00	53692.085	0.99(4)	3.9(1)	-0.4(1)	11.33(9)	1.71(5)	6.49(7)	6.52(4)	0.96(2)	1.20(78)	8.76/3.61
91435-01-01-01	53693.074	0.97(5)	3.8(1)	-0.37(9)	9.80(7)	1.70(2)	6.26(8)	6.45(5)	0.81(3)	0.99(78)	7.92/2.99
91435-01-01-02	53693.986	1.00(1)	4.2(2)	-0.6(1)	9.91(8)	1.69(3)	6.32(8)	6.46(4)	0.90(1)	0.79(78)	7.97/3.08
92030-02-01-00	53921.301	1.01(2)	3.03(2)	2.00 <sup>b</sup>	7.71(7)	1.72(7)	4.31(4)	6.41(7)	0.90(2)	1.12(78)	6.41/2.37
92030-02-02-000	53921.366	1.01(3)	2.96(1)	2.00 <sup>b</sup>	8.38(9)	0.99(2)	3.69(3)	6.45(4)	0.89(1)	1.14(78)	7.01/2.59
92030-02-03-02	53939.313	1.00(1)	3.05(3)	2.00 <sup>b</sup>	6.65(6)	0.97(3)	4.75(1)	6.45(3)	0.97(6)	1.20(78)	5.73/2.23
92030-02-03-00	53939.439	1.00(2)	2.99(1)	2.00 <sup>b</sup>	6.94(5)	0.98(4)	3.17(3)	6.47(4)	0.90(1)	0.95(78)	5.85/2.23

**Table 4**  
(Continued)

Observational ID	MJD (day)	$\alpha = \Gamma - 1$	$T_e$ (keV)	$\log(A)^b$	$N_{\text{COMPTB}}^c$	$T_s$ (keV)	$N_{\text{body}}^c$	$E_{\text{line}}$ , (keV)	$N_{\text{line}}^c$	$\chi^2_{\text{red}} (\text{dof})$	$F_1/F_2^d$
92030-02-03-01	53939.875	1.01(4)	3.02(2)	2.00 <sup>b</sup>	6.05(7)	0.99(2)	2.53(5)	6.46(5)	0.91(2)	1.16(78)	5.26/1.98
92030-02-11-000	53953.255	1.00(2)	3.00(2)	2.00 <sup>b</sup>	5.37(9)	0.83(4)	2.81(2)	6.86(2)	0.94(1)	1.00(78)	4.68/1.82
91151-04-01-00	53959.950	1.01(3)	3.10(2)	0.27(2)	6.78(5)	1.75(5)	3.74(6)	6.45(4)	1.03(7)	1.07(78)	5.32/2.06
91151-04-02-00	54028.232	1.01(4)	3.53(3)	-0.07(9)	9.86(7)	1.86(3)	5.51(8)	6.49(6)	0.90(1)	1.12(78)	7.65/2.96
92030-02-04-00	54125.301	1.03(5)	3.12(2)	2.00 <sup>b</sup>	4.32(3)	0.99(8)	4.15(2)	4.85(4)	0.90(2)	1.06(78)	3.89/1.54
92030-02-05-00	54256.402	1.00(1)	3.07(1)	2.00 <sup>b</sup>	4.24(2)	0.99(4)	3.37(3)	6.85(6)	0.87(7)	1.14(78)	3.81/1.50
92030-02-06-00	54257.346	0.99(4)	3.15(8)	2.00 <sup>b</sup>	4.25(6)	0.83(7)	2.32(1)	5.99(7)	0.90(5)	1.21(78)	3.79/1.47
92030-02-06-01	54257.452	1.01(2)	3.16(2)	2.00 <sup>b</sup>	4.22(4)	0.82(5)	2.31(1)	6.85(3)	0.88(2)	1.10(78)	3.91/1.52
92030-02-07-00	54258.447	1.04(4)	3.06(8)	2.00 <sup>b</sup>	5.35(5)	0.81(3)	2.30(2)	6.81(5)	0.78(2)	0.79(78)	4.79/1.80
92030-02-10-00	54297.188	1.02(3)	3.15(2)	2.00 <sup>b</sup>	3.74(3)	0.80(4)	2.31(2)	6.85(3)	0.95(3)	1.01(78)	3.58/1.44
92030-02-09-00	54306.346	1.00(1)	3.06(8)	2.00 <sup>b</sup>	5.35(6)	0.84(2)	2.30(3)	6.82(4)	0.91(4)	1.15(78)	3.45/1.36
94090-01-01-00	54947.682	1.02(3)	11.09(4)	-0.35(5)	2.98(3)	0.83(3)	1.79(2)	5.83(5)	2.83(3)	1.21(78)	2.01/1.63
94090-01-01-01	54947.939	1.00(2)	10.28(5)	-0.34(4)	2.79(2)	0.82(4)	1.78(3)	5.65(4)	2.89(1)	1.04(78)	1.94/1.62
94090-01-01-02	54948.728	1.03(4)	10.31(4)	-0.36(6)	2.75(1)	0.86(3)	1.79(4)	6.45(5)	2.83(2)	1.18(78)	1.89/1.66
94090-01-01-03	54948.987	0.99(3)	10.61(6)	-0.17(5)	2.66(1)	0.89(2)	1.78(6)	6.46(4)	2.82(1)	1.04(78)	1.76/1.77
94090-01-01-04	54949.708	1.01(2)	10.12(3)	-0.05(5)	3.00(2)	0.81(4)	1.79(5)	6.47(3)	2.83(3)	1.09(78)	1.89/1.73
94090-01-01-05	54950.686	1.00(1)	10.01(4)	-0.16(4)	2.65(1)	0.80(3)	1.76(9)	6.45(2)	2.85(2)	1.03(78)	1.69/1.79
94090-01-02-00	54956.589	1.02(3)	17.80(7)	0.12(1)	2.83(1)	1.78(5)	1.43(1)	6.35(4)	1.10(1)	1.09(78)	1.58/2.14
94090-01-02-03	54956.769	1.01(4)	16.44(7)	0.11(1)	2.75(2)	1.57(2)	1.44(1)	6.31(4)	1.12(3)	1.17(78)	1.59/2.08
94090-01-02-04	54957.489	1.00(2)	16.92(8)	0.27(2)	2.67(1)	1.62(3)	1.43(3)	6.38(5)	1.19(2)	1.09(78)	1.52/2.05
94090-01-02-01	54957.626	1.03(4)	17.31(9)	0.21(3)	2.61(1)	1.57(4)	1.41(2)	6.37(8)	1.11(2)	1.08(78)	1.50/2.00
94090-01-02-02	54958.664	1.00(2)	20.47(9)	0.01(2)	2.69(2)	1.69(3)	1.40(5)	6.34(4)	1.16(2)	1.10(78)	1.49/2.08
94090-01-03-00	54960.585	0.97(5)	20.3(1)	0.01(1)	2.56(1)	1.56(2)	1.44(8)	6.34(5)	1.10(9)	1.04(78)	1.41/2.00
94090-01-04-00	54978.287	1.00(2)	12.54(9)	0.47(4)	3.04(1)	1.43(6)	1.43(2)	6.36(4)	3.07(3)	1.10(78)	1.78/2.60
94090-01-04-01	54978.485	1.01(3)	11.32(4)	0.56(9)	3.04(5)	1.39(2)	1.44(3)	6.33(3)	3.08(2)	1.49(78)	1.80/2.63
94090-01-04-02	54978.749	0.99(2)	12.51(4)	0.67(8)	2.94(3)	1.73(9)	1.45(1)	6.38(4)	3.01(6)	0.99(78)	1.72/2.68
94090-01-04-03	54979.271	1.00(1)	14.96(5)	0.47(3)	2.87(2)	1.71(8)	1.43(2)	6.48(6)	3.07(4)	0.97(78)	1.67/2.56
94090-01-05-01	54980.781	1.00(3)	14.34(5)	0.54(9)	3.04(4)	1.40(2)	0.53(1)	6.42(2)	1.08(5)	0.96(78)	1.96/2.60
94090-01-05-00	54981.669	1.02(4)	13.25(4)	0.56(7)	3.15(5)	1.53(4)	1.44(2)	6.39(4)	3.14(9)	0.98(78)	1.84/2.76
94090-02-01-00	54994.514	0.97(4)	8.13(5)	-0.08(4)	4.72(5)	1.40(5)	2.54(3)	6.41(4)	1.06(7)	0.96(78)	3.18/2.96
94090-02-01-01	54997.718	1.00(2)	3.09(2)	0.42(5)	8.48(9)	1.41(2)	5.46(5)	6.45(3)	0.90(5)	0.93(78)	6.78/2.47
94090-02-02-00	55002.625	0.99(4)	3.12(2)	0.41(3)	8.98(7)	1.40(2)	6.46(7)	6.46(2)	0.91(2)	0.96(78)	6.99/2.65
92030-02-12-00	55080.709	1.01(2)	2.98(3)	2.00 <sup>b</sup>	7.18(9)	0.83(5)	4.11(4)	6.86(6)	0.87(3)	1.19(78)	6.13/2.38
92030-02-12-01	55082.884	1.00(1)	3.01(2)	2.00 <sup>b</sup>	7.15(8)	0.85(3)	5.44(6)	6.87(3)	0.89(4)	1.16(78)	6.14/2.36
92030-02-12-02	55082.647	0.98(4)	3.05(2)	2.00 <sup>b</sup>	7.50(9)	0.87(2)	4.75(4)	5.98(4)	0.90(3)	1.15(78)	6.38/2.60
92030-02-12-03	55082.581	1.01(2)	2.99(4)	2.00 <sup>b</sup>	7.07(6)	0.82(4)	4.61(9)	6.15(2)	0.97(4)	1.10(78)	6.09/2.33
92030-02-12-04	55082.773	0.96(6)	3.07(3)	2.00 <sup>b</sup>	7.32(6)	0.81(3)	4.28(8)	6.84(4)	0.91(2)	0.99(78)	6.20/2.62
92030-02-13-00	55088.379	1.01(1)	3.09(4)	2.00 <sup>b</sup>	5.58(9)	0.88(2)	4.45(9)	6.85(5)	0.97(3)	1.06(78)	5.07/1.91
92030-02-14-00	55116.958	1.02(4)	3.09(2)	2.00 <sup>b</sup>	4.52(4)	0.83(3)	3.44(4)	6.89(8)	0.94(5)	1.11(78)	4.06/1.57

**Notes.** Parameter errors correspond to a 90% confidence level.

<sup>a</sup> The spectral model is wabs\*(Blackbody + CompTB + Gaussian), where  $N_{\text{H}}$  is fixed at a value  $3.00 \times 10^{21} \text{ cm}^{-2}$  (Bloser et al. 2000); color temperature  $T_s$  and  $T_{\text{BB}}$  are fixed at 1.3 and 0.7 keV, respectively (see comments in the text).

<sup>b</sup> When parameter  $\log(A) \gg 1$ , this parameter is fixed at 2.0 (see comments in the text).

<sup>c</sup> Normalization parameters of Blackbody and CompTB components are in units of  $10^{-2} \times L_{39}/d_{10}^2 \text{ erg s}^{-1} \text{ kpc}^{-2}$ , where  $L_{39}$  is the source luminosity in units of  $10^{39} \text{ erg s}^{-1}$ ,  $d_{10}^2$  is the distance to the source in units of 10 kpc and the Gaussian component is in units of  $10^{-2} \times \text{total photons cm}^{-2} \text{ s}^{-1}$  in line.

<sup>d</sup> Spectral fluxes ( $F_1/F_2$ ) in units of  $\times 10^{-9} \text{ erg s}^{-1} \text{ cm}^{-2}$  for (3–10) and (10–60) keV energy ranges, respectively.

We use the broadband energy spectra of *BeppoSAX* (Boella et al. 1997) and *RXTE* (Bradt et al. 1993), combined with the high-timing resolution of *RXTE*, to study short- and long-term spectral and timing evolution of atoll sources.

### 3. SPECTRAL ANALYSIS

Unlike the past analyses of the source spectral data discussed in Section 1, in our study we make use of a unified model for both soft and hard states. In this way, we have an opportunity to compare the X-ray spectra of 4U 1820–30 in all states.

In our spectral model, we use an assumption that the accretion material passes through the accretion disk (for example, through the standard Shakura–Sunyaev disk; Shakura & Sunyaev 1973) and the transition layer (TL; Titarchuk et al. 1998) where soft

photons coming from the disk and NS surface are Comptonized off hot plasma (see also Figure 2 in ST12). The ground-based observer can also observe directly some fraction of these disk and NS seed photons.

Thus, our input model is a sum of the Comptonization component (COMPTB), which is the XSPEC contributed model<sup>7</sup> (see Farinelli et al. 2008, hereafter F08) and the soft BB and line (Gaussian) components. The parameters of the COMPTB component are the seed photon temperature  $kT_s$ , the electron (plasma) temperature  $kT_e$ , the energy index  $\alpha$  ( $=\Gamma - 1$ ) of the Comptonization spectrum, the illumination fraction of the Comptonized region (TL),  $f$  [ $f = A/(1 + A)$ ], and the

<sup>7</sup> <http://heasarc.gsfc.nasa.gov/docs/software/lheasoft/xanadu/xspec/models/comptb.html>

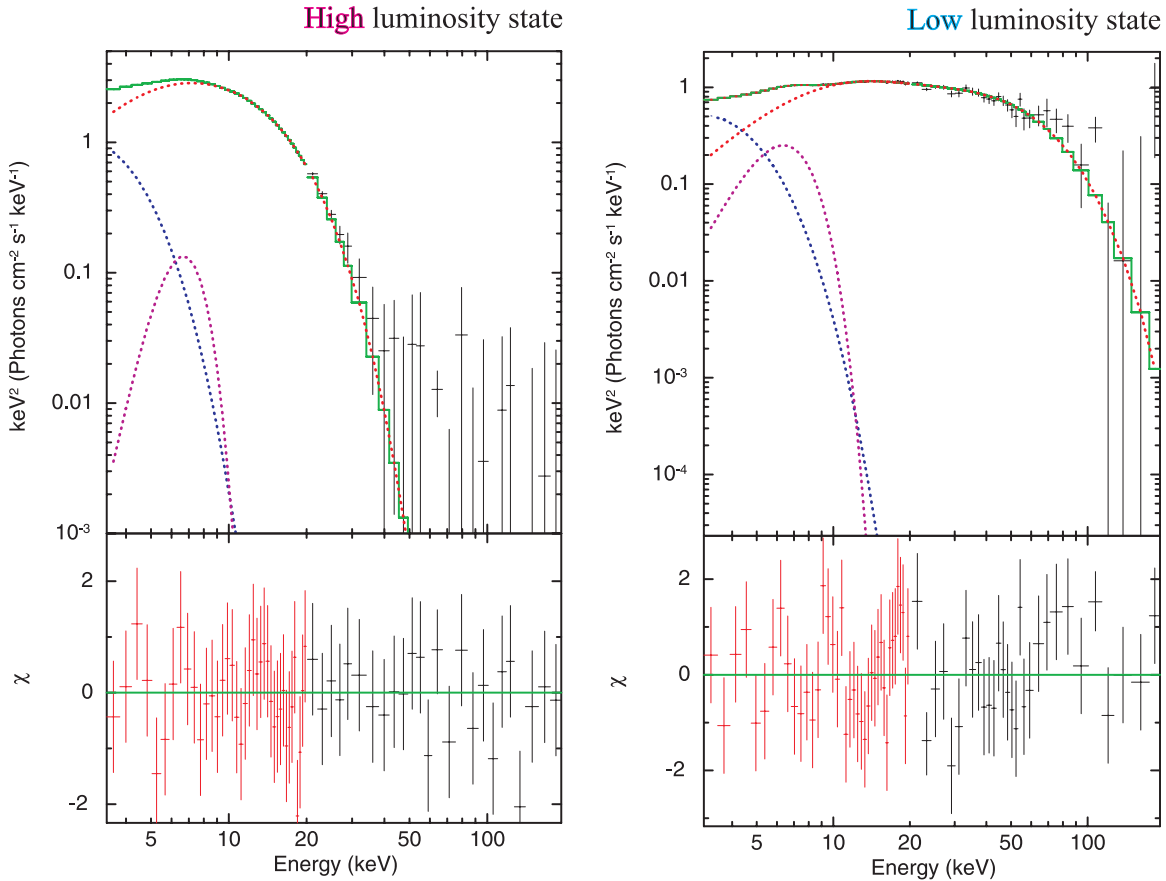


**Figure 3.** Examples of typical  $E * F(E)$  spectral diagram of 4U 1820–30 during soft (left panel) and hard (right panel) state events. The best-fit *RXTE* spectra (top panels) using the model wabs\*(Blackbody + CompTB + Gaussian) with  $\Delta\chi$  (bottom panels) for the high-luminosity (banana) state (40017-01-11-00 observation,  $\chi^2_{\text{red}} = 1.00$  for 78 dof, left panel) and for the low-luminosity (island) state (94090-01-04-00 observation,  $\chi^2_{\text{red}} = 1.10$  for 78 dof, right panel). The best-fit model parameters are  $\Gamma = 1.99 \pm 0.02$ ,  $kT_e = 2.94 \pm 0.01$  keV, and  $E_{\text{Gauss}} = 6.53 \pm 0.06$  keV (for the soft state) and  $\Gamma = 2.00 \pm 0.04$ ,  $kT_e = 12.54 \pm 0.09$  keV, and  $E_{\text{Gauss}} = 6.35 \pm 0.04$  keV (for the hard state) (see more details in Table 4). Blue, red, and violet lines indicate Blackbody, CompTB, and Gauss components, respectively.

(A color version of this figure is available in the online journal.)

normalization of the seed photons illuminating the Comptonized region,  $N_{\text{COMPTB}}$ . We include a Gaussian component in the model characterized by the parameters  $E_{\text{line}}$ ,  $\sigma_{\text{line}}$ , and  $N_{\text{line}}$  which are a centroid line energy, the line width, and the normalization, respectively. We also include a BB component and the interstellar absorption in our model characterized by the following parameters: the normalization  $N_{\text{BB}}$ , the color temperature  $T_{\text{BB}}$ , and a column density  $N_{\text{H}}$ , respectively.

We fix the index of the seed photon spectrum at  $\alpha = 2$  (or  $\gamma = \alpha + 1 = 3$ ). Namely, we suggest that this seed photon spectrum is BB-like. We neglect the bulk inflow effect with respect to the thermal Comptonization, assuming that a bulk parameter  $\delta = 0$ . The parameter  $\log(A)$  of the COMPTB component is fixed at 2 because the best-fit  $\log(A) \gg 1$ . Then  $f = A/(1+A)$  as the illumination fraction parameter is approximately 1 for any  $\log(A) \gg 1$ . We use a value of  $N_{\text{H}} = 3.00 \times 10^{21} \text{ cm}^{-2}$ , estimated by Bloser et al. (2000) for 4U 1820–30. We find satisfactory fits using our model for both *BeppoSAX* and *RXTE* observations of 4U 1820–30 for all available data sets.

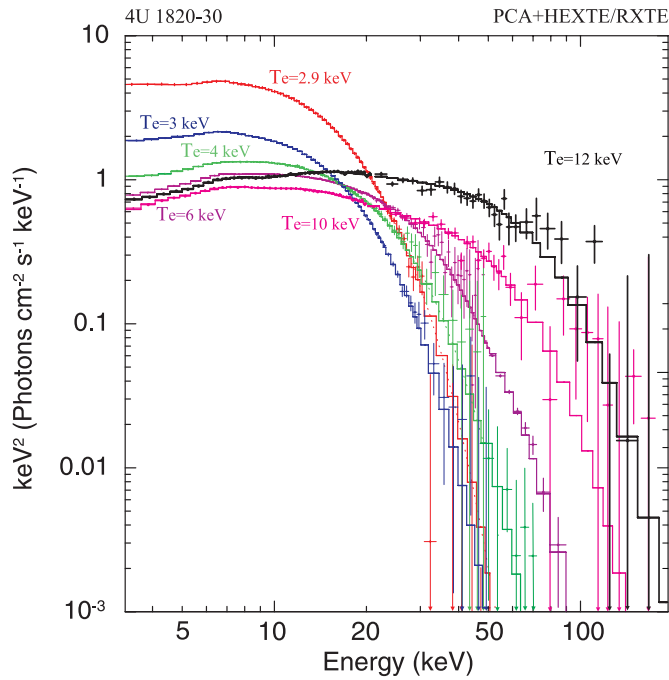
### 3.1. BeppoSAX Data Analysis

Table 3 shows the data analysis results for the broadband *BeppoSAX* spectra. On the top of Figure 2 we present an example of the *BeppoSAX* spectrum along with its best-fit using our model, while in the bottom panel we demonstrate  $\Delta\chi$  (reduced  $\chi^2 = 1.11$  for 364 dof). The line emission is

clearly centered around 6.7 keV. We find that the width of this line—0.8 keV—is quite large and is much wider than the instrumental response whose width is smaller than 0.02 keV.<sup>8</sup> This broad emission line at 6.7 keV can be a result of illumination of highly ionized iron by the X-ray continuum. Piraino et al. (2000) suggest that this broad line originates either in an ionized innermost disk region or in a hot corona above the disk. A combination of two absorption edges related to ionized iron, instead of a Gaussian line, can also describe this part of the spectrum (D’Ai et al. 2006). The *Laor* relativistically smeared line or reflection models can also be used to describe this line feature (see Ng et al. 2010 and Egron et al. 2011, respectively). However, Seifina & Titarchuk (2011) demonstrate that the model, wabs\*(Blackbody+COMPTB+Gaussian), which includes a Gaussian iron line, can successfully fit the data for extensive *RXTE* and *BeppoSAX* observations of 4U 1728–34.

We can interpret this broad iron line detected in 4U 1820–30 in terms of reprocessing emission by a disk. In addition, we fit a smeared absorption edge in the 7–8 keV range using the smedge XSPEC model (see Ebisawa et al. 1994). The edge energy is  $7.7 \pm 0.5$  keV for the wabs\*(Blackbody + CompTB + Gaussian) \* smedge model which indicates the presence of ionized material in the emission region. The smearing width is fixed at 10 keV.

<sup>8</sup> See [ftp://heasarc.gsfc.nasa.gov/sax/cal/responses/98\\_11](http://heasarc.gsfc.nasa.gov/sax/cal/responses/98_11).



**Figure 4.** Six representative  $EF_E$  spectral diagrams which are related to different electron temperatures of the TL [ $kT_e = 2.9$  keV (red), 3 keV (blue), 4 keV (green), 6 keV (violet), 10 keV (pink), and 12 keV (black)] using the model  $wabs *$  (Blackbody + CompTB + Gaussian) for island–banana state transitions of 4U 1820–30. The data are taken from *RXTE* observations 30057-01-04-01 (red), 70030-03-07-020 (blue), 70030-03-05-02 (green), 70030-03-05-01 (violet), 40017-01-24-00 (pink), and 94090-01-04-00 (black).

(A color version of this figure is available in the online journal.)

We include this edge component in the fits for all *BeppoSAX* data (see Table 3).

We obtain  $\alpha = 1.03 \pm 0.04$  (or  $\Gamma = \alpha + 1 = 2.03 \pm 0.04$ ) for all analyzed *BeppoSAX* data; the seed photon temperature  $kT_s$  of the COMPTB component is mildly variable and its value is around 1.3 keV, whereas  $kT_{BB}$  varies in the interval from 0.58 to 0.69 keV (see Tables 1 and 3 for details).

### 3.2. RXTE Data Analysis

For all *RXTE* fits, we fix the BB temperature  $kT_{BB} = 0.7$  keV. This value is an upper limit in our analysis of the *BeppoSAX* data (see Table 3), because *RXTE* detectors cannot give us reliable spectra below 3 keV. In Table 4, we show the best-fit parameters of the *RXTE* spectra using our model. It is important to point out that for all *RXTE* observations of 4U 1820–30 the photon index  $\Gamma$  only changes slightly around 2 ( $\Gamma = 1.99 \pm 0.02$ ), while the best-fit  $kT_e$  varies in the 2.5–21 keV range.

However, the determination of the iron line profile using the *RXTE* data is difficult because of the low-energy resolution of the PCA/*RXTE* detector. Moreover, the inclusion of a smedge component in the spectral model for *RXTE* data does not improve the fit quality any more. Therefore, we apply our spectral model to *RXTE* data using a simple Gaussian as the line component without smedge modeling. The line width  $\sigma_{line}$  does not vary much and it is always in the interval from 0.9 to 1.3 keV during all spectral transitions. Therefore, we fix  $\sigma_{line}$  at 1.2 keV for all spectra during the fitting procedure. The values of the best-fit seed photon temperatures,  $kT_s = 1$ –1.3 keV, are consistent with those obtained using the *BeppoSAX* data (see Table 3).

In Figure 3, we show the representative examples of the  $E * F(E)$  spectral diagrams of 4U 1820–30 during the soft

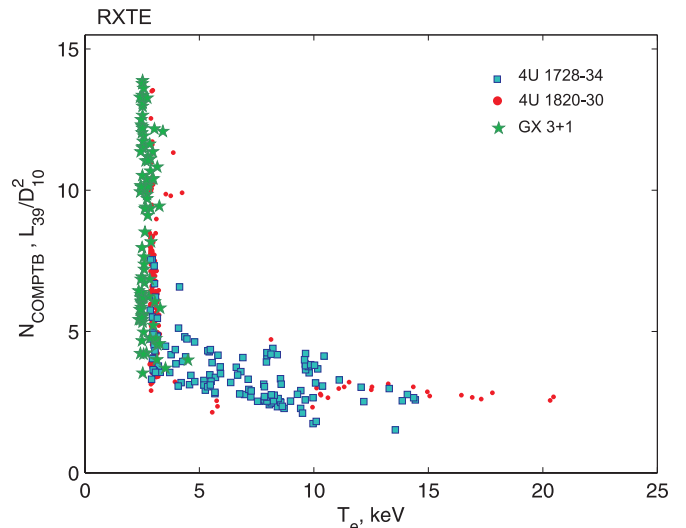


**Figure 5.** CompTB normalization measured in units of  $L_{39}^{\text{soft}} / D_{10}^2$  vs. the electron temperature  $kT_e$  (in keV) obtained using the best-fit spectral model  $wabs *$  (Blackbody + CompTB + Gaussian) for atoll sources 4U 1820–30 (red), GX 3+1 (green, taken from ST12), and 4U 1728–34 (blue, taken from ST11) for *RXTE* data.

(A color version of this figure is available in the online journal.)

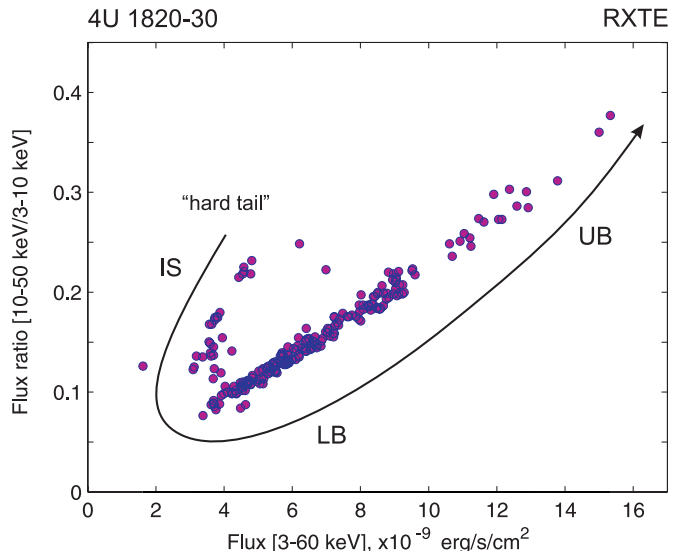


**Figure 6.** Flux ratio [10–50 keV/3–50 keV] vs. flux in the range of 3–60 keV of 4U 1820–30 for *RXTE* data. The spectral branches have been indicated for the island state (IS), lower banana state (LB), and upper banana (UB) state. The direction of the IS → LB → UB transition is indicated by the arrow. Note that  $kT_e$  decreases from 21 keV to 2.9 keV along the direction of the arrow.

(A color version of this figure is available in the online journal.)

(left panel) and the hard (right panel) state events. The best-fit *RXTE* spectra (top panels) in the model  $wabs *$  (Bbody + CompTB + Gaussian) with  $\Delta\chi$  (bottom panels) for the high-luminosity (banana) state [40017-01-11-00 observation,  $\chi^2_{\text{red}} = 1.00$  for 78 dof, left panel] and for the low-luminosity (island) state [94090-01-04-00 observation,  $\chi^2_{\text{red}} = 1.10$  for 78 dof, right panel] are also shown. The model best-fit parameters are  $\Gamma = 1.99 \pm 0.02$ ,  $kT_e = 2.94 \pm 0.01$  keV, and  $E_{\text{Gauss}} = 6.53 \pm 0.06$  keV for the soft state;  $\Gamma = 2.00 \pm 0.04$ ,  $kT_e = 12.54 \pm 0.09$  keV, and  $E_{\text{Gauss}} = 6.35 \pm 0.04$  keV for the hard state (see Table 4 for details). Violet, blue, and red lines correspond to the Gaussian, BB, and CompTB components, respectively.

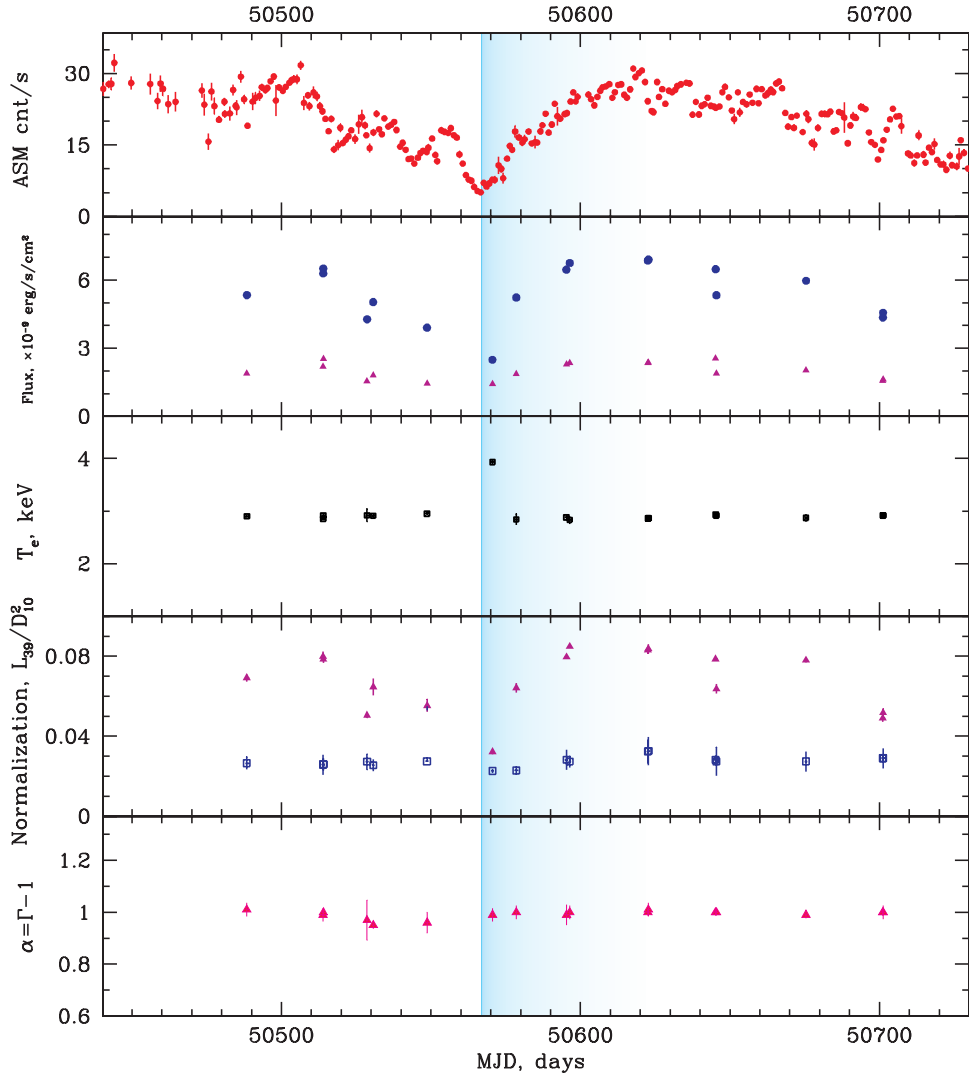


**Figure 7.** From top to bottom: evolution of the *RXTE*/ASM count rate, the model flux in 3–10 keV and 10–50 keV energy ranges (blue and crimson points, respectively), the electron temperature  $kT_e$  in keV, and CompTB and Blackbody normalizations (crimson and blue, respectively) during the 1996–1997 transition set (R1–R2). The rising phases of the local (mild) transitions are marked with blue vertical strips.

(A color version of this figure is available in the online journal.)

In Figure 4, to illustrate the spectral evolution 4U 1820–30, we show six representative  $EF_E$  spectral diagrams for different electron temperatures of a Compton cloud [ $kT_e = 2.9$  keV (red), 3 keV (blue), 4 keV (green), 6 keV (violet), 10 keV (pink), and 12 keV (black)] applying the wabs \* (Blackbody + COMPTB + Gaussian) model during island–banana state transition.

We show how the TL electron temperature  $kT_e$  anti-correlates with the normalization  $N_{\text{COMPTB}}$  (proportional to  $\dot{M}$ ) in Figure 5. For a comparison, we add the points for 4U 1728–34 and GX 3+1 (see Seifina & Titarchuk 2011 and Seifina & Titarchuk 2012, respectively). The electron temperature  $kT_e$  decreases and saturates at about 3 keV when the mass-accretion rate increases (see an explanation of this effect in Farinelli & Titarchuk 2011; hereafter FT11).

Our spectral model applied to the spectral data of *BeppoSAX* and *RXTE* is robust in all the data sets. Namely, a value of reduced  $\chi^2_{\text{red}} = \chi^2/N_{\text{dof}}$ , where  $N_{\text{dof}}$  is a number of degrees of freedom, is around 1.0 for most of the observations.  $\chi^2_{\text{red}}$  is about 1.5 for less than 3% of the spectra with high counting statistics but  $\chi^2_{\text{red}}$  is never above a rejection limit of 1.6. Note that the high residuals of the poor-fit spectra (2 among 234 spectra for

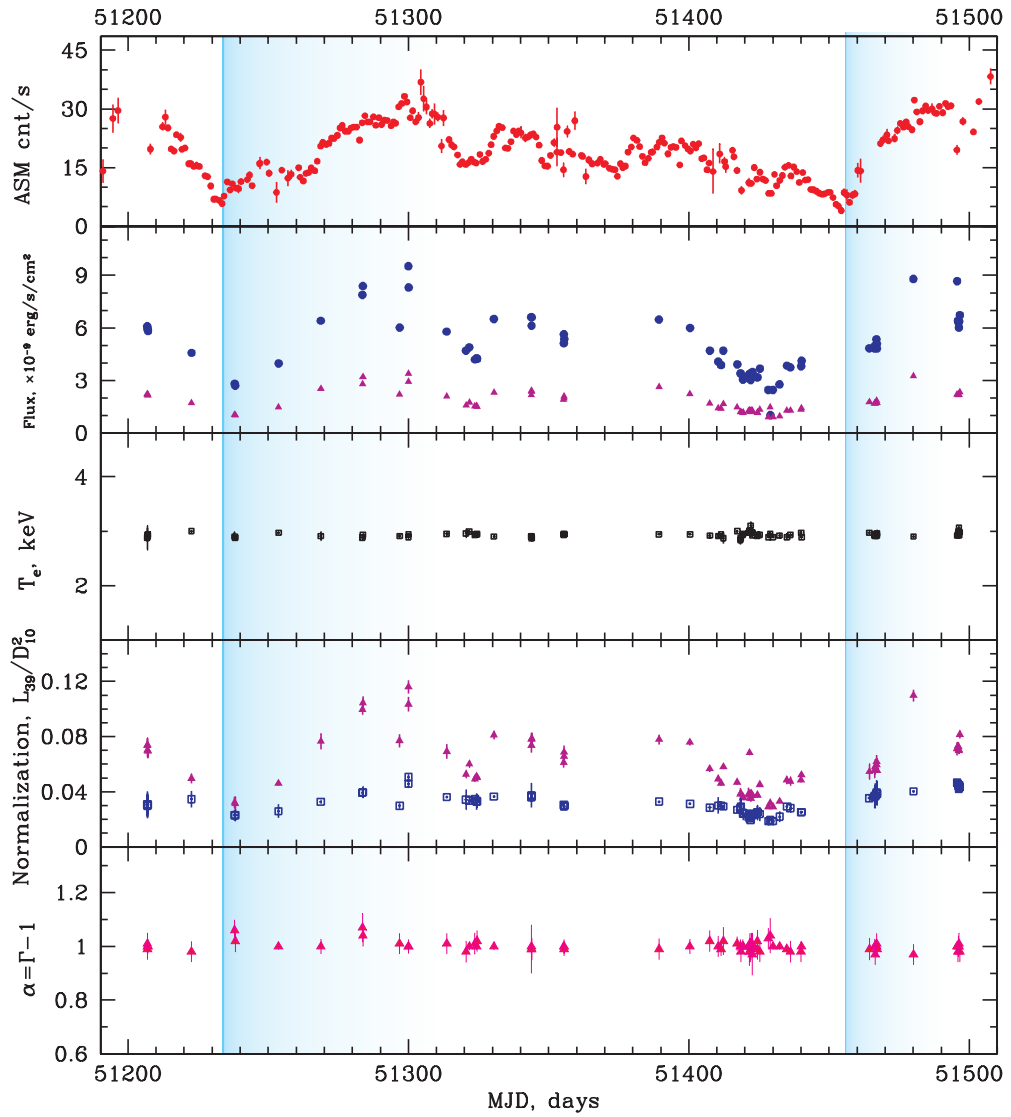
which  $\chi^2 = 1.55$ ) occur in the iron line region. As was shown by the *BeppoSAX* analysis, the shape of the iron line is more complex than a simple Gaussian (see discussion in Section 3.1). Probably, the fits of this line indicate a broad line, whose shape and width are a result of scattering of the line photons in the hot plasma (TL) along with the iron smedge effect there. However, we cannot resolve this line complexity using the *RXTE* data.

Thus using broadband *BeppoSAX* observations, we can obtain the best-fit parameters of our spectral model. Due to the large-time coverage of 4U 1820–30 by *RXTE*, we are capable of studying the source spectral transitions in the 3–200 keV energy range.

## 4. OVERALL PATTERN OF X-RAY PROPERTIES

### 4.1. Hardness–Intensity Diagram

To study the properties of 4U 1820–30 during the spectral transitions when the luminosity changes, we use hard color (10–50 keV/3–50 keV) (HC) versus the 3–60 keV flux measured in units of  $10^{-9}$  erg s $^{-1}$  cm $^{-2}$  (hardness–intensity

**Figure 8.** Similar to Figure 7 but for the *RXTE* 1999 transition set R3.

(A color version of this figure is available in the online journal.)

diagram, HID). In Figure 6, we show the flux ratio HC versus the 3–60 keV flux using the *RXTE* data. As it appears from this figure, 4U 1820–30 shows a “J”-like diagonal shape in this diagram with upper short and lower elongated branches, which are joined at the lowest flux point. The spectral branches are indicated for the island state (IS), the lower banana state (LB) and the upper banana (UB) state. The direction of the IS→LB→UB transition is shown by an arrow. The electron temperature  $kT_e$  changes from 21 keV to about 3 keV along the direction of the arrow (compare with Figure 5).

The identification of HID states is made using simultaneous timing and spectral analysis, and we have revisited the previous similar *RXTE* data analysis made by Bloser et al. (2000) and Migliari et al. (2004).

In particular, the HC drops from 0.25 to 0.1 while the 3–60 keV flux is quasi-constant when the source propagates from the IS toward the LB. On the other hand, the HC rises from 0.12 to 0.35 with a simultaneous growth of the 3–60 keV flux when the source goes further from the LB toward the UB.

## 5. EVOLUTION OF X-RAY SPECTRAL PROPERTIES DURING SPECTRAL STATE TRANSITIONS

A number of X-ray spectral transitions of 4U 1820–30 with luminosity variations have been detected by *RXTE* during 1996–2009 (*R1–R7* sets). We investigate common spectral-timing signatures that can be found for these spectral transition events. The source reveals different behaviors during high-luminosity and low-luminosity events.

### 5.1. Evolution of X-Ray Spectral Properties during High-luminosity Events

In Figures 7 and 8, we show the results of our spectral analysis of the *RXTE* observations applying the wabs \* (Blackbody + COMPTB + Gaussian) model. In the top panels, we present the *RXTE*/ASM count rate and the model fluxes from 3 to 10 keV and from 10 to 50 keV (see blue and crimson points, respectively). The TL electron temperature  $kT_e$  as a function of time is shown in the third panel from the top. The temperature  $kT_e$  changes in the 2.9–4 keV interval during the

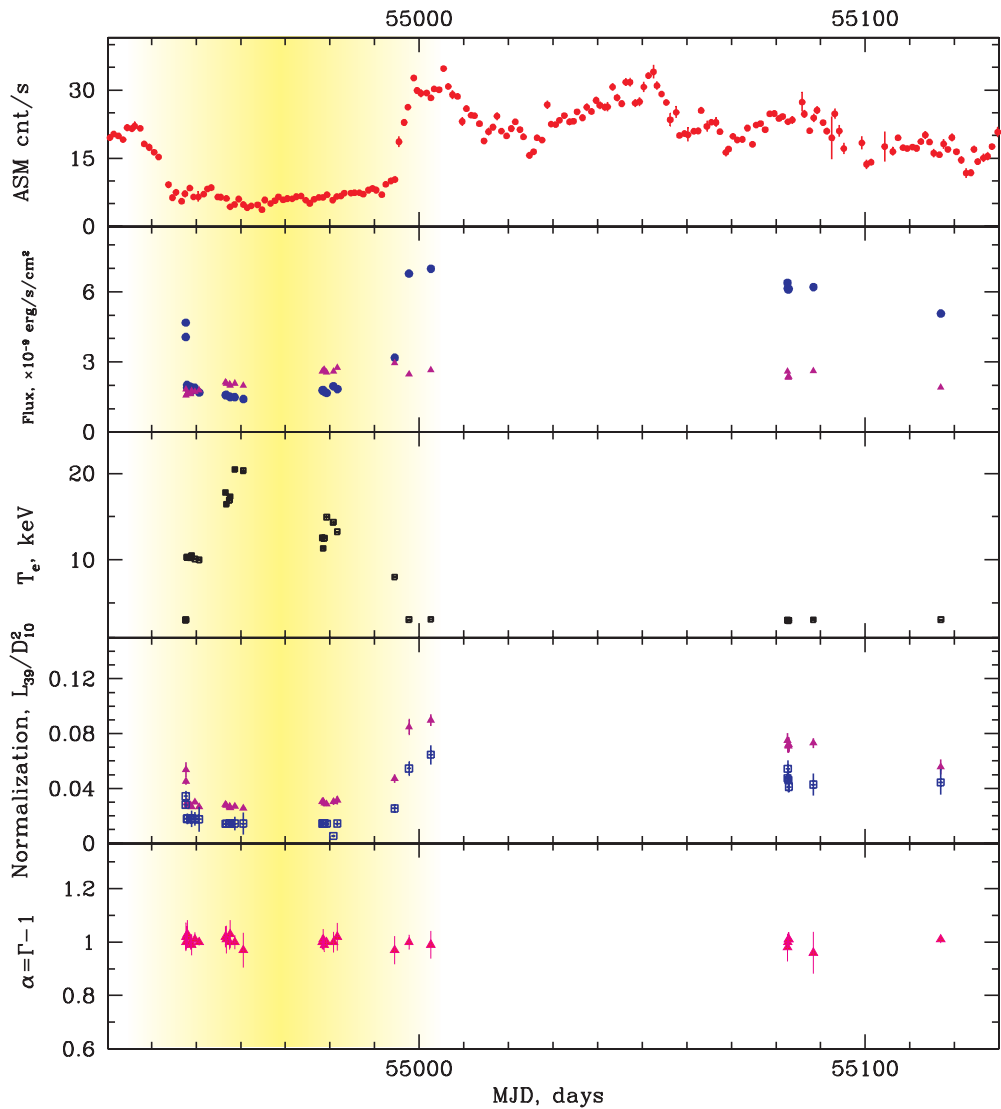


**Figure 9.** Similar to Figure 7 but for the *RXTE* 2009 transition set R7. The quasi-plateau phases of the low-luminosity state of 4U 1820–30 are marked using orange vertical strips.

(A color version of this figure is available in the online journal.)

time period MJD 50490–MJD 50700 and only slightly varies around 3 keV during the MJD 51200–MJD 51500 time interval. The COMPTB normalization  $N_{\text{COMPTB}}$  and the normalization of the low-temperature BB component  $N_{\text{BB}}$  (crimson and blue points, respectively) are presented in the second-to-bottom panels of Figures 7 and 8. One can clearly see that the COMPTB normalization  $N_{\text{COMPTB}}$  correlates with variations of the ASM count rate and the 3–10 keV model flux. On the other hand, the BB normalization  $N_{\text{BB}}$  only slightly varies.

### 5.2. Evolution of X-Ray Spectral Properties during the Low-luminosity Events

Since late April of 2009, 4U 1820–30 showed a prominent X-ray low-hard state at energies less than 10 keV as it was observed by the X-ray monitors on *RXTE* and *Swift*. We display the characteristics of the low-hard state obtained using the *RXTE* data in Figure 9. Since 2009 April 24 (MJD 54945), the source was steadily brightening in the 15–50 keV band of the *Swift*/Burst Alert Telescope (BAT), with a daily average of  $0.032 \pm 0.002$  counts  $\text{cm}^{-2} \text{s}^{-1}$  (145 mCrab; Krimm et al.

2009). In contrast, the highest count rate detected by the *Swift*/BAT was 0.14 counts  $\text{cm}^{-2} \text{s}^{-1}$ .

The ASM/*RXTE* and PCA/*RXTE* light curves showed that 4U 1820–30 was in an extended low state from MJD 54944 to MJD 54982. The ASM count rate took a sharp drop at MJD 54944 while the flux began rising in the BAT monitor. The ASM count rate was very low, approximately  $6.0 \pm 0.5$  counts  $\text{s}^{-1}$  during this low-state period, with respect to a usual average count rate of  $\sim 20$  counts  $\text{s}^{-1}$ . During the same time period, the *RXTE*/PCA count rate decreased from  $\sim 4000$  counts  $\text{s}^{-1}$  to  $\sim 1000$  counts  $\text{s}^{-1}$ . This kind of long-time low state was not observed from 4U 1820–30 over the 10–15 year period. The typical low-state duration varies from 1 to 2 weeks.

We also establish that the X-ray spectra of this source over the low-luminosity state (MJD 54955–54982) are quite stable in terms of the CompTB normalization value. But the electron temperature  $kT_e$  of the Comptonized plasma increases from 3 keV up to 20 keV during the MJD 54950–54960 period and after that  $kT_e$  gradually decreases again to 3 keV when the luminosity rises at the end of the quasi-plateau (at MJD 55000). In Table 4, we report the best-fit parameter values. During the

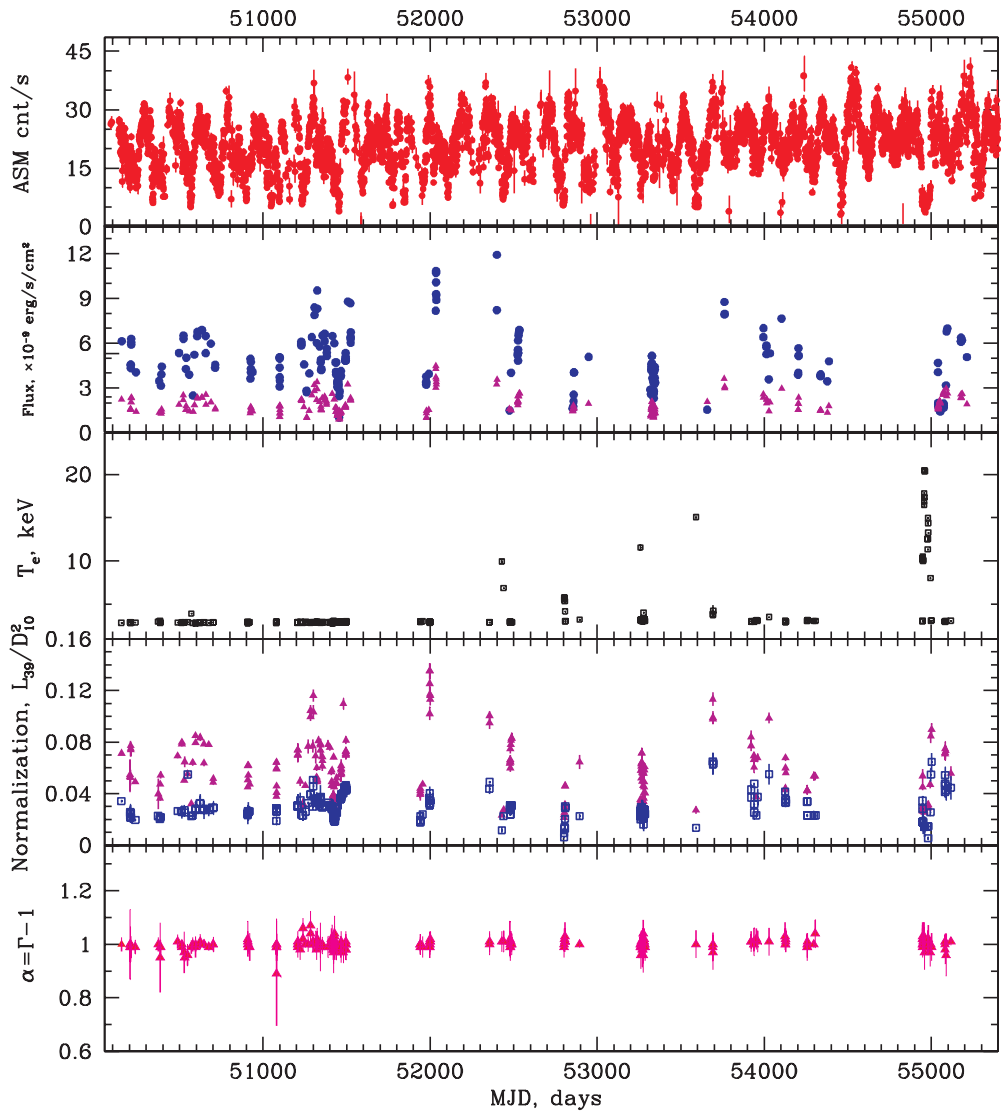


**Figure 10.** Same as Figure 7 but for all *RXTE* sets (*R1–R7*) to demonstrate a long-time variability.  
(A color version of this figure is available in the online journal.)

IS-B transition period, we find that the photon index  $\Gamma$  (or the spectral index  $\alpha = \Gamma - 1$ ) is almost constant; i.e., it only slightly varies around 2 (see the combined Figure 10).

### 5.3. Spectral State Transitions in 4U 1820–30

In 4U 1820–30, the hard–soft state transition is observed as  $kT_e$  decreases from 15–20 keV to 3 keV (see Figure 9). The outburst hard-to-soft state transitions are seen when the soft photon flux  $N_{\text{COMPTB}}$  dramatically increases (see Figures 5 and 6). In general, following FT11, we consider the spectral state transitions in terms of the  $kT_e$  change. Thus, the hard state is seen when the electron temperature reaches a maximum,  $kT_e^{\max}$ , whereas the soft state is observed when the electron temperature,  $kT_e^{\min}$  reaches a minimum. Note that  $kT_e$  is well determined by the high-energy cut-off of the spectrum,  $E_{\text{cut}}$ , and can be well established by the spectral fits to the data. This spectral state definition is based on  $kT_e$  (or  $E_{\text{cut}} \sim 2kT_e$ ). Unlike what occurs in the case of NS binaries, for a black hole (BH) case one can relate a spectral state change to the spectral (photon) index change (see Shaposhnikov & Titarchuk 2009, hereafter ST09).

We test the hypothesis of  $\Gamma_{\text{appr}} \approx 2$  using a  $\chi^2$ -statistic criterion. We calculate the distribution of  $\chi^2_{\text{red}}(\Gamma_{\text{appr}}) = (1/N) \sum_{i=1}^N (\Gamma_i - \Gamma_{\text{appr}}/\Delta\Gamma_i)^2$  versus  $\Gamma_{\text{appr}}$  and we find a sharp minimum of the function  $\chi^2_{\text{red}}(\Gamma_{\text{appr}})$  at 1 when  $\Gamma_{\text{appr}} = 1.99 \pm 0.01$  and  $\Gamma_{\text{appr}} = 1.99 \pm 0.02$  with confidence levels of 67% and 99% for 234 dof, respectively, (see the related figure of  $\chi^2_{\text{red}}(\Gamma_{\text{appr}})$  for 4U 1728–34 in ST11). The index  $\Gamma$  is almost constant when  $kT_e$  (see Figure 11) and the COMPTB normalization,  $L_{39}/d_{10}^2$ , change (see below). Based on an analysis of *BeppoSAX* data, FT11 proposed that  $\Gamma$  is about 2 for quite a few NS sources. FT11 also define the spectral state using a value  $kT_e$  and they demonstrate that  $\Gamma = 2 \pm 0.2$  (or  $\alpha = 1 \pm 0.2$ ) when  $kT_e$  varies in the 2.9–21 keV interval.

It should be noted that not all NSs show spectral state transitions but quite a few NSs do exhibit them. For instance, so-called atoll-sources (such as 4U 1820–30) usually demonstrate IS-B transitions. Particularly during such transitions, it can be possible to distinguish an NS from a BH. Specifically, NSs and BHs show drastically different variations of spectral characteristics. NSs, examples of which include 4U 1820–30 and 4U 1728–34, indicate variabilities of  $kT_e$  and mass-accretion

**Table 5**  
Comparison of the Parameters of atoll Sources 4U 1820–30, GX 3+1<sup>1</sup>, and 4U 1728–34<sup>2</sup>

Source	D (kpc)	Type of Donor Star	Mass of Donor Star ( $M_{\odot}$ )	$P_{\text{orb}}$ (minute)	i (deg)	$kT_e$ (keV)	$N_{\text{COMPTB}}$ ( $L_{39}^{\text{soft}}/D_{10}^2$ )	$kT_{\text{BB}}$ (keV)	$kT_s$ (keV)	f	$t_{\text{LS-HS-LS}}$ (days)
GX 3+1	4.5 <sup>3</sup>	A	~ 10	...	...	2.3–4.5	0.04–0.15	0.6	1.16–1.7	0.2–0.9	1000
4U 1820–30	5.8–8 <sup>4</sup>	WD	0.07	$11.46 \pm 0.04$	$43 \pm 9^5$	2.9–21.0	0.02–0.14	0.6	1.1–1.7	0.2–1	170
4U 1728–34	4.2–6.4 <sup>6</sup>	?	...	...	...	2.5–15	0.02–0.09	0.6–0.7	1.3	0.5–1	15

**References.** (1) ST12; (2) ST11; (3) Kuulkers & van der Klis 2000; (4) Shaposhnikov & Titarchuk 2004; (5) Arons & King 1993; (6) van Paradijs 1978.

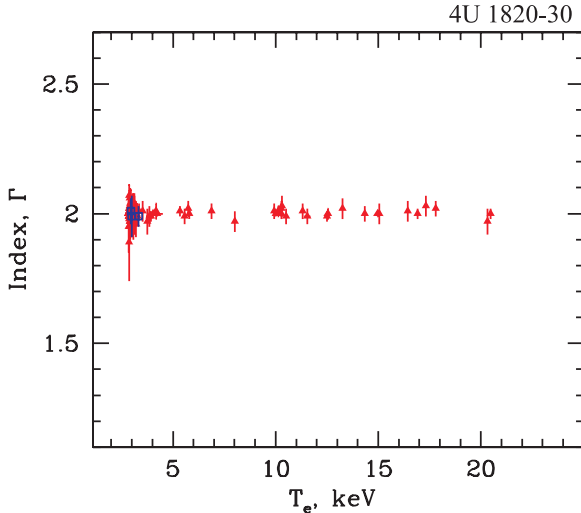


**Figure 11.** Photon index  $\Gamma$  vs. electron temperature  $kT_e$  (in keV) in the frame of our spectral model wabs \* (Blackbody + CompTB + Gaussian) during transition events (see Tables 3 and 4). Blue and red points correspond to *BeppoSAX* and *RXTE* observations, respectively.

(A color version of this figure is available in the online journal.)

rate  $\dot{M}$  along with a quasi-constant index  $\Gamma$  equal to about 2. Meanwhile, BHs demonstrate a monotonic growth of  $\Gamma$  when  $\dot{M}$  increases and reaches its final flattening (saturation; see ST09).

## 6. SPECTRAL–TIMING CORRELATIONS DURING SPECTRAL STATE TRANSITIONS

We analyze the *RXTE* light curves applying the *powspec* task taken from FTOOLS 5.1. We implement the timing analysis *RXTE/PCA* data which we perform in the 13–30 keV range applying the *event* mode with a time resolution of  $1.2 \times 10^{-4}$  s. We make power density spectra (PDS) in the 0.1–500 Hz frequency range with a 0.001 s time resolution. The Poissonian statistic’s contribution was subtracted. We apply the QDP/PLT package<sup>9</sup> for PDS modeling.

### 6.1. Spectral and Timing Properties during the Low-luminosity State Transition

In Figure 12, we present the generic behavior of X-ray timing–spectral characteristics for the low-luminosity state at R7 (2009) transition events. We plot PDSs (left column) along with the  $E * F(E)$ –spectral diagram (right column) for six moments at MJD = 54947.6/54956.5, 54958.6/55002.6, and 54997.7/54960.36, covering different transition phases. At the bottom, we demonstrate PDSs for the 15–30 keV energy range (left column) and plot these along with the  $E * F(E)$ –spectral

diagram (right column) for A–C time events (see upper panel). All points [(events) A red (ID 94090-01-01-00), A blue (ID 94090-01-02-03), B red (ID 94090-01-02-02), C red (ID 94090-01-04-03)], except B (blue) and C (red), are related to the IS (broadband noise, no VLFN).

PDSs denoted by B (blue, ID 94090-02-02-00) and C (red, ID 94090-0103-00) exhibit the island–lower-banana state transition. For the blue PDS the VLFN (very low frequency noise) appears as a BLN component that transforms into a QPO (a broad Lorentzian with a  $v_h$  centroid frequency at 7–10 Hz). We present PDS (panels A1, B1, C1) along with corresponding  $E * F(E)$ –spectral diagrams (panels A2, B2, C2). The related PDSs and energy spectral data are shown by blue and red points, respectively. In the left panel, we also show the electron temperature  $kT_e$  associated with a given PDS.

### 6.2. Spectral and Timing Properties during the High-luminosity State Transition

To compare with Figure 12, we show the evolution of spectral–timing characteristics during the high-luminosity state in Figure 13. In the top panel, we display the ASM light curve during the high-luminosity interval at R3 (1999) transition events. Red/blue points A, B, and C are related to the moments at MJD = 51283.6/51300, 51313.7/51330.5, and 51389.4/51396.26 covering different transition phases. In the bottom left and bottom right panels, we present PDSs for the 15–30 keV energy range and the  $E * F(E)$ –spectral diagram respectively, for the A (red, top), B (blue, middle), and C (blue, bottom) points of the X-ray light curve (see the upper panel). All points are related to the banana state with relatively strong broadband noise and VLFN with QPOs at  $v_l \sim 6$ –7 Hz for the C moment (red). The PDSs in panel C (blue and red) illustrate the island–lower-banana state transition. Here the VLFN appears and the BLN component transforms into a QPO (a broad Lorentzian with  $v_h$  centroid frequency at 7–10 Hz, C red, 40017-01-12-00). The power spectra (panels A1, B1, C1) correspond to  $E * F(E)$  diagrams (panels A2, B2, C2). The corresponding energy spectra of 4U 1820–30 are related to the electron temperature of 3 keV.

In Figure 14, we illustrate a typical power spectrum of 4U 1820–30 for different X-ray spectral states (shown in the right panel). The electron temperature values of corresponding energy spectra are indicated on the right vertical axis. The power spectra in the extreme island state (EIS), IS (multiplied by factor  $10^{-2}$  for clarity), lower left banana state (LLB,  $\times 10^{-4}$ ), lower banana state (LB,  $\times 10^{-6}$ ), and upper banana state (UB,  $\times 10^{-8}$ ) are presented from the top to the bottom. The histograms show the best fits to the power spectra, which consist of three components: VLFN the peaked noise component, low-frequency QPOs ( $v_l$  and  $v_h$ ) and the high-frequency feature  $v_{\text{hHz}}$  (see van Straaten et al. 2003 for details of the terminology).

<sup>9</sup> <http://heasarc.gsfc.nasa.gov/ftools/others/qdp/qdp.html>

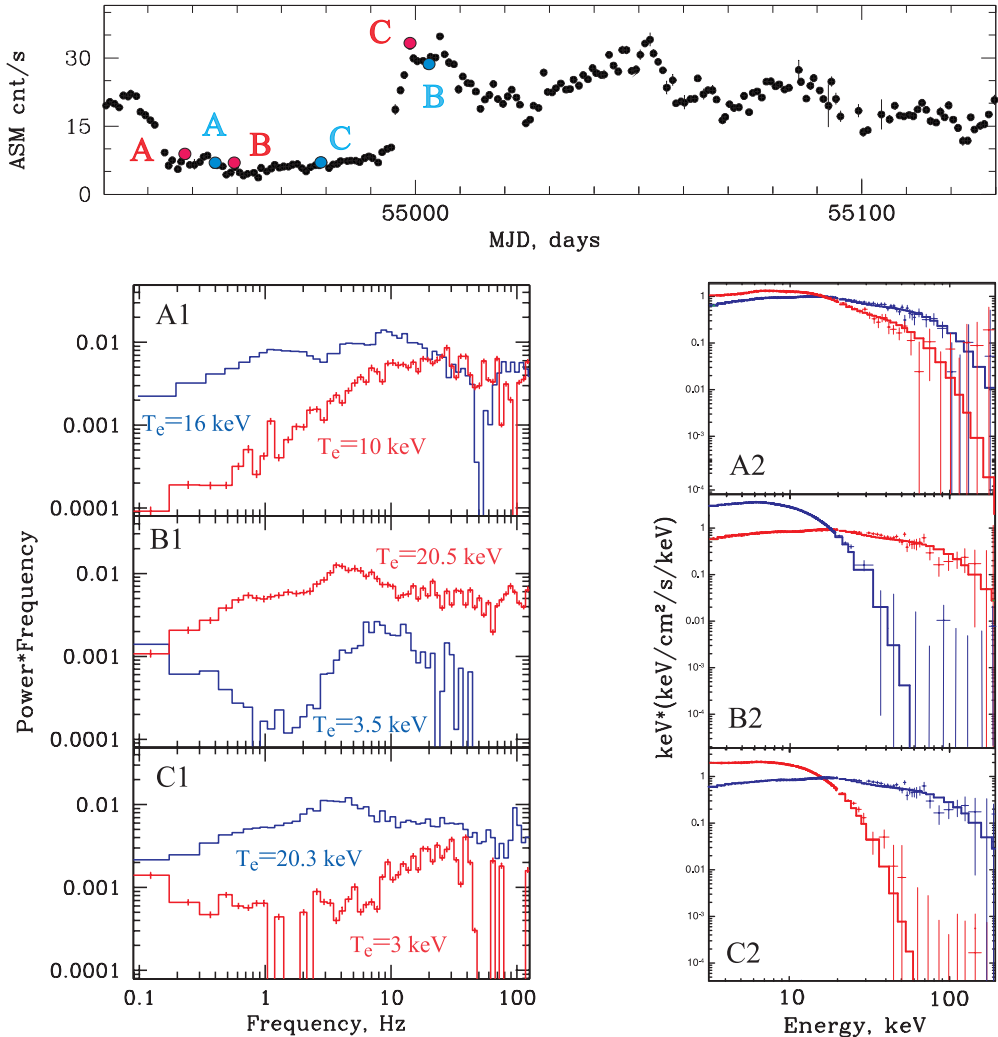


**Figure 12.** Top: evolution of the *RXTE*/ASM count rate during low-luminosity state R7 (2009) transition events. Red/blue points A, B, and C mark moments at MJD = 54947.6/54956.5, 54958.6/55002.6, and 54997.7/54960.36 covering different transition phases. Bottom: PDSs for the 15–30 keV band (left column) are plotted along with the  $E * F(E)$ -diagrams (right column) for A, B, and C points of the X-ray light curve. The  $E * F(E)$ -diagrams (panels A2, B2, C2) are related to the corresponding power spectra (panels A1, B1, C1). The data shown by blue and red points are related to the corresponding power spectra. In the left bottom panel, we indicate  $kT_e$  related to a given PDS.

(A color version of this figure is available in the online journal.)

### 6.3. Comparison of Spectral and Timing Characteristics of atoll Sources 4U 1820–30, GX 3+1, and 4U 1728–34

In this paper, we also study the correlations of X-ray spectral–timing characteristics and  $\dot{M}$  in a number of atolls during their spectral transitions. We search for similarities and differences between atoll sources. In this way, we can present a comparative analysis of three atoll sources: 4U 1820–30, GX 3+1, and 4U 1728–34. We apply the same spectral model that consists of a low-temperature BB, a Comptonized continuum, and Gaussian line components.

#### 6.3.1. Constancy of the Photon Index

We demonstrate that atolls 4U 1820–30, GX 3+1, 4U 1728–34 show a similar pattern of photon index  $\Gamma$  versus  $\dot{M}$  (or  $N_{\text{COMPTB}}$ ). Namely, the photon index  $\Gamma$  only slightly varies around 2 (see Figure 15). Following FT11, ST11, and ST12, we can suggest that the cooling flow of soft disk photons is much less than the energy release in the TL for each of these three sources.

#### 6.3.2. The Differences and Similarities of $kT_e$ Ranges in 4U 1820–30, GX 3+1, and 4U 1728–34

One can see from Figure 16 that the ranges of  $kT_e$  for an individual state evolution of these three sources are different. The electron temperature  $kT_e$  changes in 4U 1728–34 from 3 to 15 keV, whereas  $kT_e$  varies within a much narrow range of  $kT_e$  around 3 keV in GX 3+1. In turn, source 4U 1820–30 demonstrates a wider interval of  $kT_e$  in which  $kT_e$  varies from 2.9 keV to 21 keV, similar to some extent to the temperature change in 4U 1728–34. Note that in a low-temperature regime, 4U 1820–30 and GX 3+1 are similar in terms of normalization  $N_{\text{COMPTB}} = (4–15) \times L_{39}/D_{10}^2$ , or mass accretion rate, (see Figure 5) and Comptonized fraction  $f = 0.2–0.8$  (see Figure 16), whereas 4U 1820–30 and 4U 1728–34 are similar for a range of the normalization  $N_{\text{COMPTB}} = (2–4) \times L_{39}/D_{10}^2$  (see Figure 5) and  $f = 0.5–0.8$  (see Figure 16) for the high-temperature regime. However, in contrast to 4U 1728–34, the source 4U 1820–30 has an additional branch of intermediate temperatures (8–12 keV) when the Comptonized fraction is

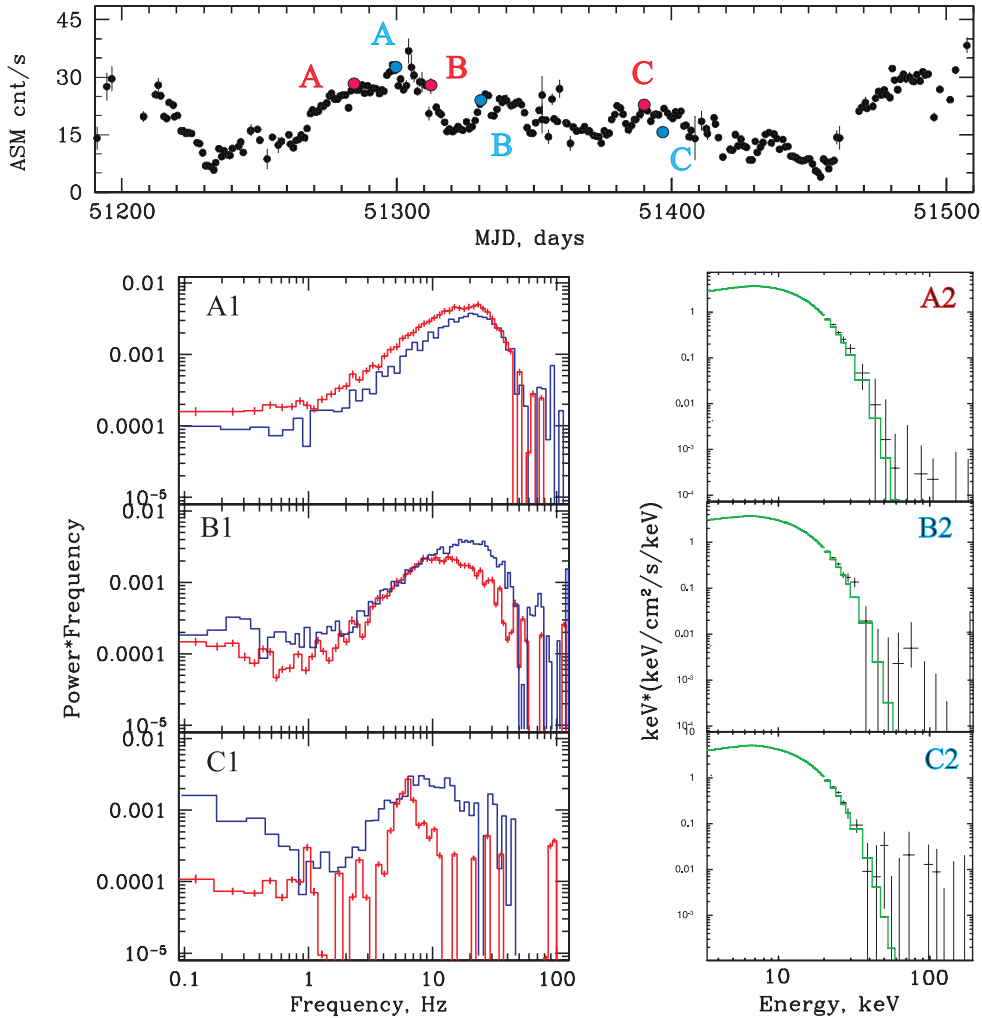


**Figure 13.** Top: evolution of the *RXTE*/ASM count rate during the high-luminosity state R3 (1999) transition events. Red/blue points A, B, and C mark moments at MJD = 51283.6/51300, 51313.7/51330.5, and 51389.4/51396.26 covering different transition phases. Bottom: PDSs for the 15–30 keV band (left column) are plotted along with the  $E * F(E)$ —diagram (right column) for A (red, top), B (blue, middle), and C (blue, bottom) points of the X-ray light curve. All points are related to the banana state [strong broadband noise, VLFN and QPOs at  $\nu_l \sim 6\text{--}7$  Hz (C red)]. The  $E * F(E)$ —diagrams (panels A2, B2, C2) are related to the corresponding power spectra (panels A1, B1, C1). The data are shown by black points. The electron temperature  $kT_e$  of the corresponding energy spectra of 4U 1820–30 is about 3 keV.

(A color version of this figure is available in the online journal.)

relatively low,  $f < 0.5$  (see Figure 16). Note that all objects have a common temperature interval 3–4 keV when  $N_{\text{COMPTB}}$  (or mass accretion rate) is relatively high.

Thus, according to FT11, ST11, ST12, and the present study, the electron temperature  $kT_e$  for atolls and Z-sources varies in the 2.5–25 keV range. Specifically, the change of  $kT_e$  around 3 keV is similar for all three source 4U 1820–30, GX 3+1, and 4U 1728–34. The minimum value of  $kT_e$  at 2.5 keV occurs at the peak luminosity for 4U 1728–34 (see ST11), during a local rise of luminosity for GX 3+1 (ST12), and at high-luminosity phases for 4U 1820–30.

For all three of these objects, the values of color seed photon temperatures  $kT_s = 1.1\text{--}1.7$  keV and BB temperatures  $kT_{\text{BB}} \simeq 0.6$  keV are comparable (see Table 5). In contrast, the variability extent of  $kT_e$  is not similar. The reason for the difference in electron temperature ranges is evident. Sources 4U 1820–30 and 4U 1728–34 show a complete cycle of state evolution: IS–LB–UB stages for 4U 1820–30 and an EIS–UB state for 4U 1728–34 EIS–UB state (see Di Salvo et al. 2001; ST11). But GX 3+1 demonstrates a short evolution behavior on

the CCD from the LB to the UB. This evolutionary picture is also clear from Figure 16 which shows that the track of GX 3+1 is only a part of the full track (see the definition of a state sequence and the standard atoll–Z scheme in Hasinger & van der Klis 1989).

Note that 4U 1820–30 shows almost the same  $kT_e$  range as that of 4U 1728–34 and an almost identical timing evolution. But clear differences between these atolls can be seen in Figure 17, where we show spectral hardness (10–50 keV/3–50 keV) versus flux in the 3–60 keV range. In fact, 4U 1728–34 (blue points) is fainter and harder and demonstrates a much wider range of spectral hardness than that of 4U 1820–30 (red points).

#### 6.3.3. Comparison of Spectral Evolution as a Function of the Luminosity for 4U 1820–30, GX 3+1, and 4U 1728–34

Now we present a comparison of X-ray spectral evolution for sources 4U 1820–30, GX 3+1, and 4U 1728–34 based on the luminosity value that is presumably proportional to

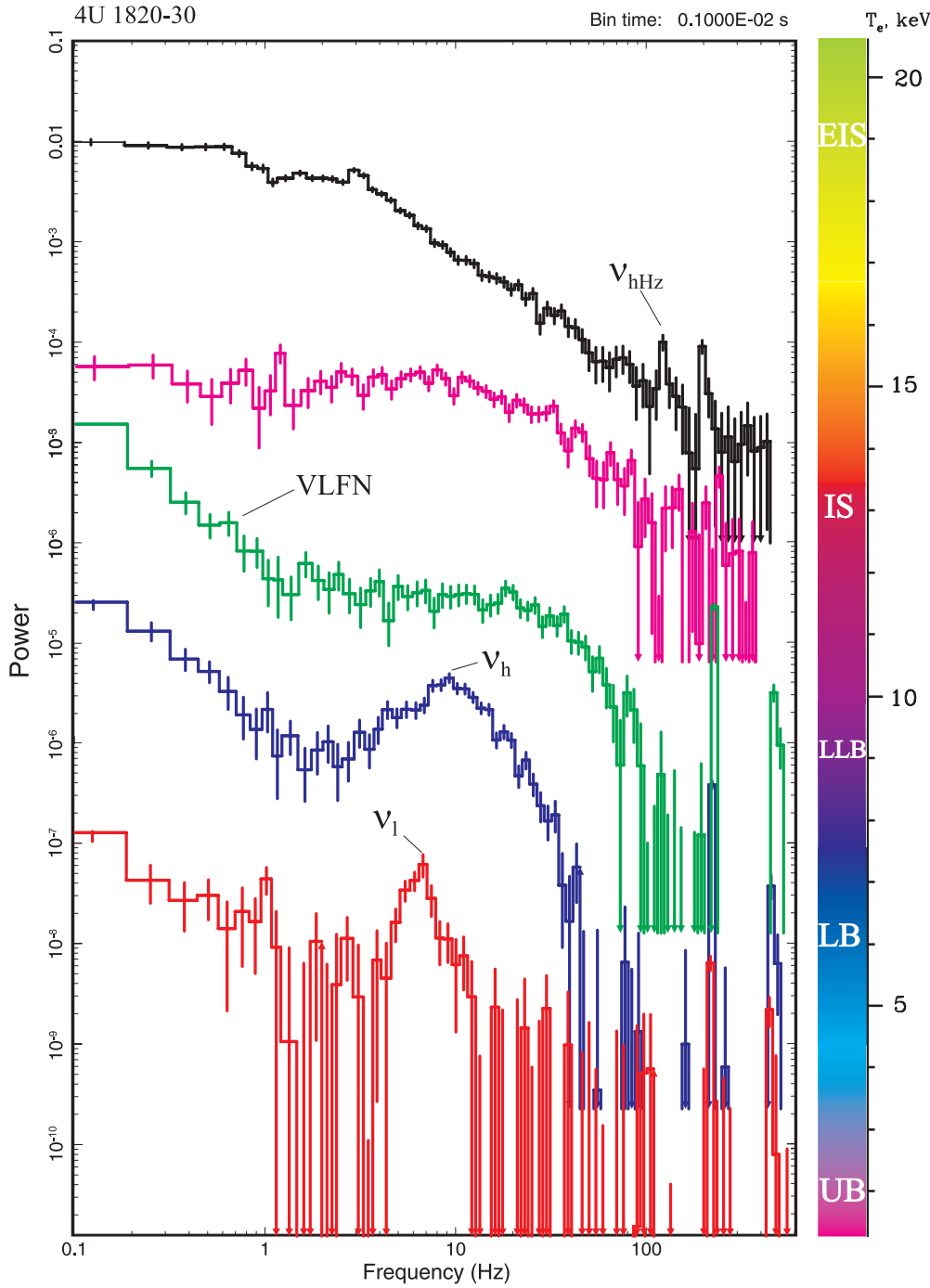


**Figure 14.** PDSs of 4U 1820–30 related to its X-ray spectral states.  $kT_e$  values (in keV) corresponding to the energy spectra are indicated on the right vertical axis. PDSs in the extreme island state (EIS), island state (IS, multiplied by a factor  $10^{-2}$  for clarity), lower left banana state (LLB,  $\times 10^{-4}$ ), lower banana state (LB,  $\times 10^{-6}$ ), and upper banana state (UB,  $\times 10^{-8}$ ) are presented from top to bottom. The histograms consist of four components: VLFN (very low frequency noise in banana states), the peaked noise component, low-frequency QPOs fit by Lorentzians ( $v_l$ ,  $v_h$ ), and high-frequency QPOs ( $v_{hHz}$ ).

(A color version of this figure is available in the online journal.)

CompTB normalization and, consequently, to the mass accretion rate (taking into account the fact that these objects' distances to the Earth are similar; see Table 5). For 4U 1820–30, the distance range is within 5.8–8 kpc (Shaposhnikov & Titarchuk 2004), whereas for 4U 1728–34 and GX 3+1 the distances are estimated as 4.5 kpc and 4.2–6.4 kpc, respectively (see van Paradijs 1978; Kuulkers & van der Klis 2000).

We show the CompTB normalization (related to the soft photon luminosity value) for these sources as a function of

$kT_e$  in Figure 5. 4U 1820–30 subtends a wider interval in CompTB normalization than that of 4U 1728–34. Note that in the high-luminosity state (or  $N_{\text{COMPTB}}$ ) 4U 1820–30 is similar to GX 3+1:  $N_{\text{COMPTB}} = (4\text{--}15) \times L_{39}/D_{10}^2$ , the Comptonized fraction  $f = 0.2\text{--}0.8$  (see Figure 16), and the electron temperatures  $kT_e$  vary little around 3 keV. While in the low-luminosity state, 4U 1820–30 is closer to source 4U 1728–34:  $N_{\text{COMPTB}} = (2\text{--}5) \times L_{39}/D_{10}^2$  (see Figure 5),  $f = 0.5\text{--}0.8$ , and  $kT_e$  changes from 5 to 20 keV (see Figure 16).

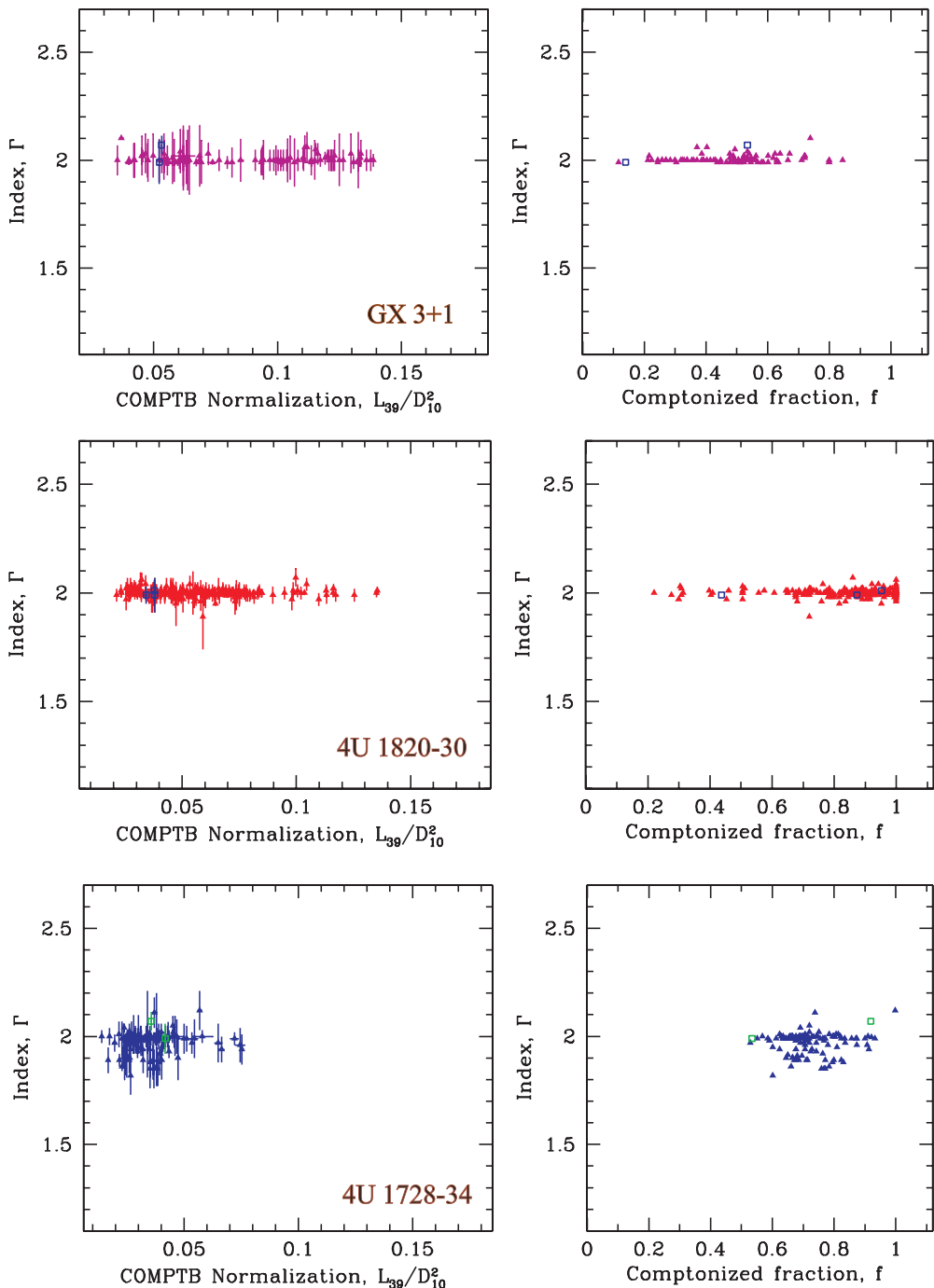


**Figure 15.** From top to bottom: plots  $\Gamma$  vs. CompTB normalization (left column) and vs. Comptonized fraction  $f$  (right column) for GX 3+1 (top), 4U 1820–30 (middle), and 4U 1728–34 (bottom) obtained using the wabs \* (Blackbody + CompTB + Gaussian) model. In the top panels, crimson and blue points are for GX 3+1 taken from ST12 and in the middle panels for 4U 1820–30 red and blue points correspond to *RXTE* and *BeppoSAX* data, respectively (current study). In the bottom panels, blue and green points correspond to *RXTE* and *BeppoSAX* data, respectively, for 4U 1728–34 (data taken from ST11).

(A color version of this figure is available in the online journal.)

#### 6.3.4. The Differences and Similarities of the Timescales of State Evolution for 4U 1820–30, GX 3+1, and 4U 1728–34

We should point out that all three of these atoll sources show transitions between low-luminosity and high-luminosity states over different timescales. Specifically, the timescales of X-ray flux variability for 4U 1728–34, 4U 1820–30, and GX 3+1 which are probably dictated by variability of mass accretion rate are  $\sim 10$  days, 100 days, and 1000 days, respectively.

However, these sources demonstrate an LB–UB transition and make this transition in the narrow interval of the low temperature  $kT_e$  (around 3 keV) and during the same short time interval (hours–day). We remind the reader that the comparison between these three sources is facilitated by the fact that they show almost the same  $kT_{BB}$  and  $kT_s$  temperature values and they are located at approximately the same distance. The only difference in spectral evolution of these objects is related to their different ranges in electron temperature of the Comptonized component.

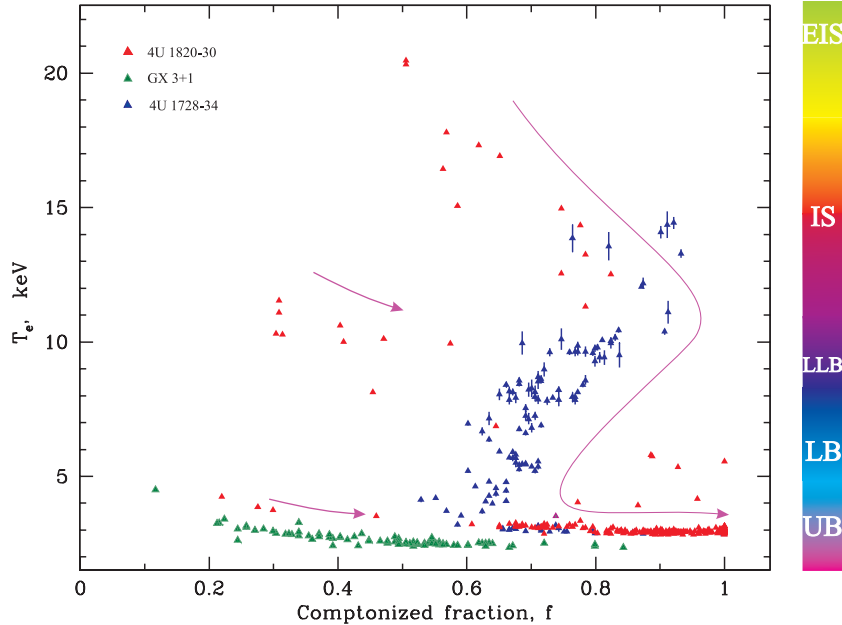


**Figure 16.**  $kT_e$  (in keV) plotted vs. illumination (comptonized) fraction  $f$  for 4U 1820–30, GX 3+1 (taken from ST12), and 4U 1728–34 (taken from ST11) during spectral state transitions obtained using the wabs \* (Blackbody + CompTB + Gaussian) model. Red, green, and blue points correspond to *RXTE* observations of 4U 1820–30, GX 3+1, and 4U 1728–34, respectively. The curved arrows are related to an increase in mass accretion rate. On the right-hand side of the figure, we show a sequence of CCD states (EIS: extreme island state; IS: island state; LLB: lower left banana state; LB: lower banana state; UB: upper banana state) which are listed according to the standard atoll–Z scheme (Hasinger & van der Klis 1989). One can see that  $kT_e$  is directly related to the sequence of CCD stages.

(A color version of this figure is available in the online journal.)

### 6.3.5. Correlation of Illumination Parameter $f$ versus Electron Temperature $kT_e$ and Its Relation with Different Stages in the Color–Color Diagram

Using Table 5, one can see that the ranges of the best-fit illumination fraction  $f$  are 0.2–1.0, 0.2–0.9, and 0.5–1 for 4U 1820–30, GX 3+1, and 4U 1728–34, respectively. These values of  $f$  indicate a different geometry of the TL and thus different illumination for these X-ray sources.

In Figure 16, we demonstrate that the electron temperature  $kT_e$  directly correlates with a sequence of CCD states, EIS-IS-LLB-LB-UB (see Hasinger & van der Klis 1989 for this CCD classification). Note that ST12 reveal a relation between spectral states,  $kT_e$ , and  $f$  for atoll sources GX 3+1 and 4U 1728–34. We show these  $kT_e-f$  relations for these two atolls in Figure 16. The direction in which the inferred  $M$  increases is indicated by arrows.

Now we present three different tracks on the  $kT_e-f$  diagram for the three sources 4U 1820–30, GX 3+1, and 4U 1728–34 and show how these tracks are related to the standard CCD sequence (see Figure 16). The track of 4U 1820–30 consists of three segments (branches) related to  $kT_e$ : high-(12–21 keV), intermediate-(7–12 keV), and low-temperature (2.9–6 keV) ones, wherein each segment has a negative correlation of  $kT_e$  and  $f$ . GX 3+1 demonstrates only the so-called low-temperature branch track. Namely, when the fraction  $f$  increases,  $kT_e$  decreases from  $\sim 4.5$  keV to  $\sim 2.3$  keV. For 4U 1728–34, we see a more complicated pattern. In contrast to 4U 1820–30 and GX 3+1, 4U 1728–34 has a segment with a positive correlation of  $kT_e$  versus  $f$  from 4 to 12 keV. Specifically, at the high-temperature state (EIS),  $f$  changes only slightly from 0.9 to 1 when  $kT_e$  decreases. As  $kT_e$  further drops from 12 keV to 4 keV,  $f$  also drops from 0.9 to 0.5. Finally,  $f$  goes up from 0.5 to 0.8 when the source enters the low-temperature state (LB-UB). As a result, we demonstrate that

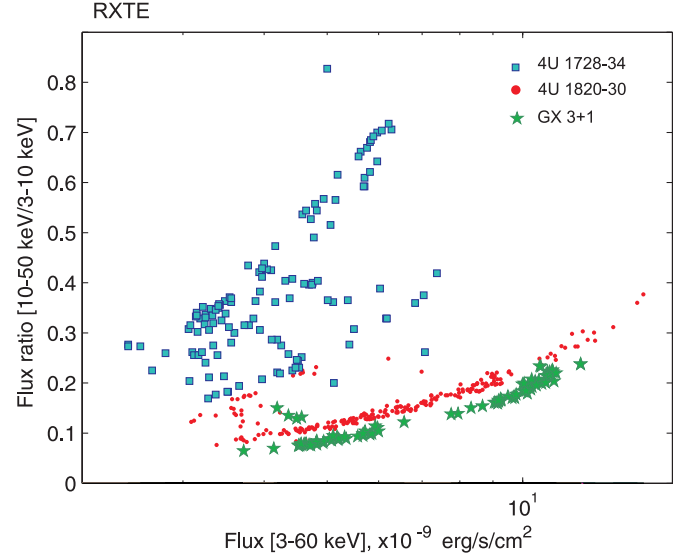


**Figure 17.** Spectral hardness (10–50 keV/3–10 keV) vs. flux in the 3–60 keV range for 4U 1820–30 (red, current study), 4U 1728–34 (blue, taken from ST11), and GX 3+1 (green, taken from ST12).

(A color version of this figure is available in the online journal.)

the CCD state evolution can also be seen using the  $kT_e-f$  correlation.

### 6.4. Comparison of Spectral Hardness Diagrams for atolls 4U 1820–30, GX 3+1, and 4U 1728–34

We use the plot HC (10–50 keV/3–50 keV) versus the 3–60 keV flux in the form of HIDs for the three sources: 4U 1820–30 (red), GX 3+1 (green), and 4U 1728–34 (blue, see Figure 17) to compare transition properties of these atolls in terms of their flux (or luminosity). In fact, 4U 1820–30 shows

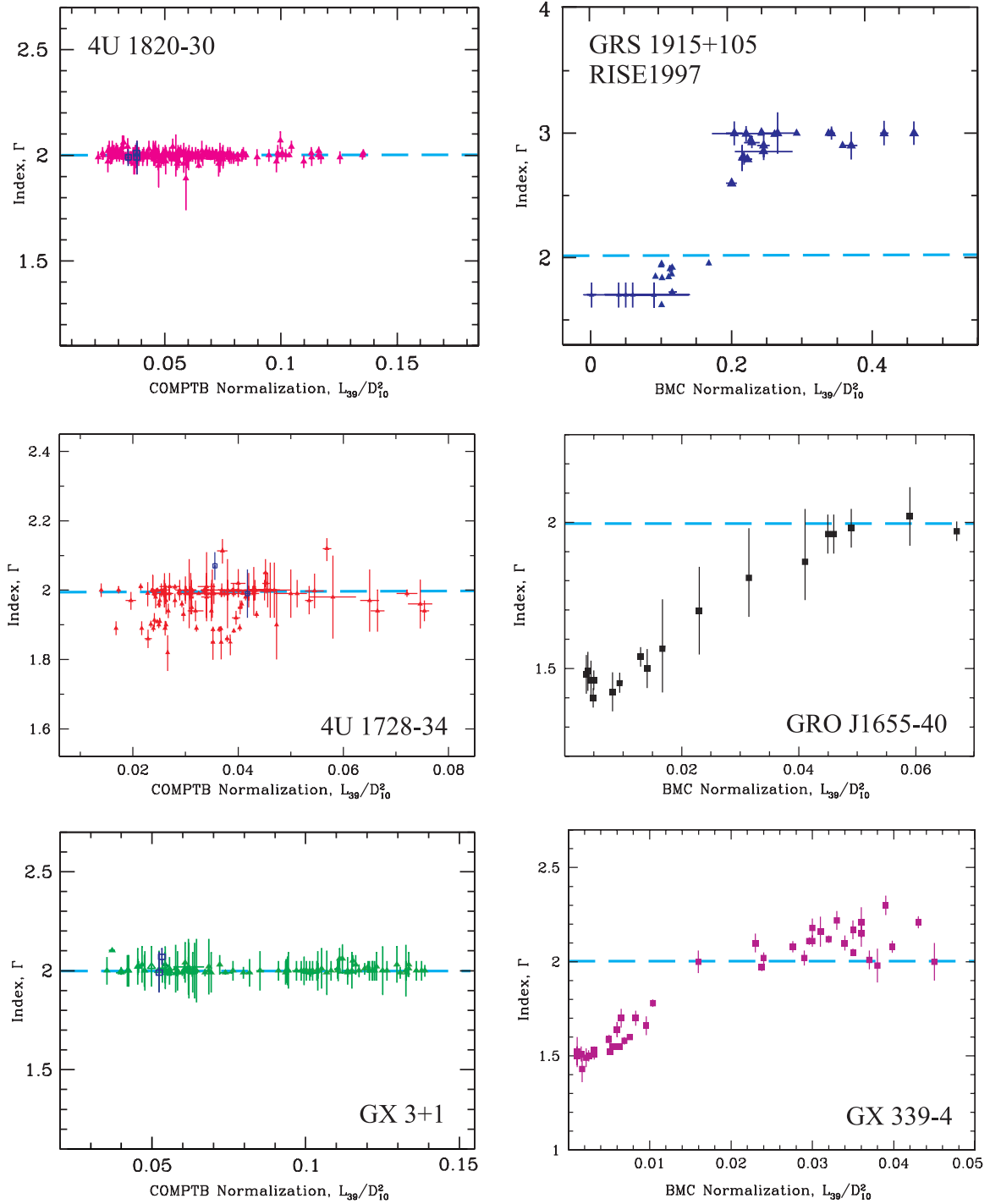


**Figure 18.** Examples of diagrams of the photon index  $\Gamma$  vs. the COMPTB normalization (proportional to mass accretion rate) for BH sources (right column, GRS 1915+105 (TS09), GRO J1655-40 (ST08), and GX 339-4 (ST08)) along with atoll NS sources (left column, 4U 1820–30, 4U 1728–34 (ST11), and GX 3+1 (ST12)). For all plots, the *RXTE* data were used along with *BepoSAX* data (indicated by blue points in the left column). One can see a noticeable change in  $\Gamma$  followed by the saturation plateau for BHs while for NSs the index only slightly varies around  $2\Gamma = 2$  is indicated by the blue dashed line.

(A color version of this figure is available in the online journal.)

a ‘J’-like inclined (or diagonal) shape in the HID with short upper and elongated lower branches (see also Figure 6). The short branch is close to the low-luminosity state, whereas the elongated branch covers a wide luminosity range.

Our comparative analysis of the HID track branches for 4U 1820–30, GX 3+1, and 4U 1728–34 indicates that these objects have similar physical properties. The spectral and timing characteristics are very similar along corresponding segments.

Specifically, the short branch of a ‘J’-like track of 4U 1820–30 is adjacent to a low-luminosity area of 4U 1728–34 (blue points) and it is related to a high electron temperature regime of 4U 1820–30, as in 4U 1728–34. In turn, the elongated branch of 4U 1820–30 is closer to the GX 3+1 (green points) branch area and it is associated with low electron temperatures  $kT_e$  (3–4 keV) and softer spectra, which are also seen in GX 3+1.

Note that among the considered atolls, superbursts are observed only in GX 3+1 and 4U 1820–30 during the elongated branch. Furthermore, superbursts are detected at low–soft states, i.e., during the low-luminosity interval of a light curve when the electron temperature  $kT_e$  is about 4 keV. Thus, 4U 1820–30 shows a property similar to GX 3+1 and it is situated at an intermediate position between 4U 1728–34 and GX 3+1 in terms of its luminosity. This observational fact can be related to the same intermediate rate of mass transfer in these two sources, 4U 1820–30 and GX 3+1. The comparison of HIDs allows us to diagnose physical properties of different objects with adjacent HID tracks.

## 7. DISCUSSION

### 7.1. Stability of the Photon Index is a Signature of an NS Source

Thus, we demonstrate that the photon spectral index only slightly varies around 2 using numerous observations of NS sources 4U 1820–30, GX 3+1 (ST12), and 4U 1728–34 (ST11) by *BeppoSAX* and *RXTE*. In Figures 11, 15, and 18 (left column) we show  $\Gamma$  as a function of the spectral model parameters:  $kT_e$  (in keV),  $N_{\text{COMPB}}$ –normalization, and illumination fraction  $f$ . These results for NS 4U 1820–30 were obtained when we applied our thermal Comptonization model to *BeppoSAX* and extensive *RXTE* observations. FT11 and ST11 performed similar investigations and found the photon (energy) index to be stable in other observations of NS binaries. We explain this index stability using the Comptonization model. Namely, the photon (energy) index is almost constant when the soft photon flux-illuminated TL is much less than the gravitational energy release in the TL (see, e.g., ST12). This model of the index stability can probably resolve the index stability effect now clearly established in these three NS sources using extensive *BeppoSAX* and *RXTE* observations.

### 7.2. On the Hard Tail Origin in atoll Source 4U 1820–30

The radio emission detected from 4U 1820–30 (Migliari et al. 2004) suggests the presence of a jet, which may also generate extended power-law X-ray emission. In this case, the power law can be a result of the inverse Compton effect on nonthermal electrons of the jet. Note, X-ray nonthermal power-law tails are also observed in soft states of BHs (see, for example, a review by ST09; see also McConnell et al. 2002 and Wardzinski et al. 2002 on the detection of the extended hard tails in the hard states of BHs, Cyg X-1, and GX 339-4 respectively, and NS Z-sources; see Di Salvo et al. 2000; Farinelli et al. 2005; D’Amico et al. 2001; Asai et al. 1994). However, these extended hard tails are also found in atolls (see, e.g., Piraino et al. 1999).

Additive models that have been applied to fit the spectra of 4U 1820–30 need to use an additional power-law component (a pure one or a component of CompPS) to describe a hard spectral tail above 80 keV (see, e.g., Tarana et al. 2006). However, such an approach invokes an unknown non-thermal origin of hard tail emission. On the other hand, our suggestion allows us to explain X-ray spectra of 4U 1820–30 in all spectral states using the same model without a specific composition of the model components at different states. In fact, in our model (see Sections 5.2 and 6.1), we describe the hard tail emission using the thermal Comptonization component in which the TL electron temperature  $kT_e$  increases up to 20 keV and the illumination factor  $f$  decreases as the source goes to the hard state (see Figures 4 and 16).

## 8. CONCLUSIONS

We analyze the X-ray spectral and timing characteristics of 4U 1820–30 observed during the hard–soft state transitions. We find a number of spectral transitions in 4U 1820–30 using *BeppoSAX* and *RXTE* data.

For our investigation, we take advantage of the *BeppoSAX* broad spectral extension over the 0.3–200 keV range and abundant *RXTE* observations taken with 3–200 keV energy coverage.

We demonstrate that the X-ray broadband spectra can be successfully fit by a combination of a Blackbody, Comptonization (CompTB), and Gaussian–line components for all spectral states. Also, we show an observable relation of the photon index  $\Gamma$  and the normalization of the Comptonized component, CompTB, which is proportional to  $\dot{M}$ . We demonstrate the stability of the photon index  $\Gamma \sim 2$  when the source goes from the hard state to the soft state, in other words, when the electron temperature of the Comptonized region (TL),  $kT_e$  decreases from 21 to 3 keV (see Figure 11).

We also show that  $\Gamma$  only slightly varies with the CompTB normalization ( $\propto \dot{M}$ ). Note, this stability of the index in NS sources has been recently suggested for a number of other NSs, Sco X-1, Cyg X-2, GX 17+2, GX 3+1, GX 340+0, GX 349+2, X 1658–298, 1E 1724–3045, and GS 1826–238, which were analyzed using *BeppoSAX* data (see details in FT11; ST11; ST12). The use of the disk seed photon normalization, (CompTB), which is proportional to  $\dot{M}$ , is fundamental in order to find the stability of  $\Gamma$  during the hard–soft state transition. We do find stability (constancy) of the photon index of the Comptonized component versus both the CompTB normalization and the electron temperature  $kT_e$  at about 2 for all spectral states. In our analysis of NS sources (see FT11; ST11; ST12; Seifina et al. 2013, and this paper) we do not find any particular case in which the photon index  $\Gamma$  changes beyond the limits  $2 \pm 0.1$ . Thus, this index stability can be taken as an intrinsic property of NS binaries (as an NS signature), which is drastically different from that of BH binaries (e.g., GX 339-4, GRO J1655-40, XTE J1650-500, XTE J1550-564, 4U 1543-47, XTE J1859+226, H 1743-322, (ST09), GRS 1915+105 (TS09), SS 433 (ST10)), where  $\Gamma$  monotonically rises during the hard–soft state transition and is followed by a saturation at high  $\dot{M}$ -values (see Figure 18). In Figure 18, we show the  $\Gamma$ – $\dot{M}$  correlation for a number of BHs (right column) and that  $\Gamma$  is almost independent of  $\dot{M}$  in NSs (left column). Indices  $\Gamma$  in BHs show a clear correlation with  $\dot{M}$  or with the normalization  $L_{39}/D_{10}^2$  (where  $L_{39}$  is the flux of soft (seed) photons). The  $\Gamma$ – $\dot{M}$  correlation is followed by  $\Gamma$ -saturation when the mass accretion rate  $\dot{M}$  exceeds the Eddington limit. The behavior of  $\Gamma$  versus  $\dot{M}$  for the considered sample of NSs (4U 1820–30, 4U 1728–34, and GX 3+1) is drastically different from that for given examples of BHs.

The relatively wide interval of the illumination fraction  $f = 0.2$ –1 that we obtain in the framework of our model points to variable soft (disk) photon illumination of the TL in 4U 1820–30. Using *BeppoSAX* data, we also find two types of BB photons. One type is characterized by a color temperature of 0.7 keV, which is typical for the disk photons, and the other one has a color temperature of 1.3 keV, which can be associated with NS surface temperatures.

We detect an evolution of 6–20 Hz QPOs and noise components during the island–banana state evolution (LLB–UB, see Figure 13).

Our observational results establishing the constancy of the photon index  $\Gamma$  in 4U 1820–30 confirm the theoretical arguments of **FT11** and **ST11** that the TL energy release  $Q_{\text{cor}}$  dominates the soft photon flux illuminating the TL which comes from the accretion disk,  $Q_{\text{disk}}$ . We argue that the stability of  $\Gamma$  we found is an intrinsic NS signature since in BH binaries  $\Gamma$  monotonically increases with  $M$  followed by a saturation at high values of  $M$  (see **ST09**).

L.T. acknowledges discussion with Chris Shrader and his thorough editing of the manuscript and the authors appreciate the comments of the referee that substantially improved the quality of the material presented.

## REFERENCES

- Arons, J., & King, I. R. 1993, *ApJL*, **413**, L121  
 Asai, K., Dotani, T., Mitsuda, K., et al. 1994, *PASJ*, **46**, 479  
 Bloser, P. F., Barret, D., Grindlay, J. E., et al. 1996, *A&AS*, **120**, 275  
 Bloser, P. F., Grindlay, J. E., Kaaret, P., et al. 2000, *ApJ*, **542**, 1000  
 Boella, G., Chiappetti, L., Conti, G., et al. 1997, *A&AS*, **122**, 327  
 Bradt, H. V., Rothschild, R. E., & Swank, J. H. 1993, *A&AS*, **97**, 355  
 Chou, Y., & Grindlay, J. E. 2001, *ApJ*, **563**, 934  
 Christian, D. J., & Swank, J. H. 1997, *ApJS*, **109**, 177  
 Clark, G. W., Li, F. K., Canizares, C., et al. 1977, *MNRAS*, **179**, 651  
 Cornelisse, R., in't Zand, J. J. M., Verbunt, F., et al. 2003, *A&A*, **405**, 1033  
 D'Ai, A., et al. 2006, *A&A*, **448**, 817  
 D'Amico, F., Heindl, W. A., Rothschild, R. E., & Gruber, D. E. 2001, *ApJL*, **547**, L147  
 Di Salvo, T., Iaria, R., Burderi, L., & Robba, N. R. 2000, *ApJ*, **542**, 1034  
 Di Salvo, T., Méndez, M., van der Klis, M., Ford, E., & Robba, N. R. 2001, *ApJ*, **546**, 1107  
 Ebisawa, K., Ogawa, M., Aoki, T., et al. 1994, *PASJ*, **46**, 375  
 Egron, E., Di Salvo, T., Burderi, L., et al. 2011, *A&A*, **530**, A99  
 Farinelli, R., Frontera, F., Zdziarski, A. A., et al. 2005, *A&A*, **434**, 25  
 Farinelli, R., & Titarchuk, L. 2011, *A&A*, **525**, 102 (FT11)  
 Farinelli, R., Titarchuk, L., Paizis, A., & Frontera, F. 2008, *ApJ*, **680**, 602 (F08)  
 Ford, E. C., van der Klis, M., Mendez, M., et al. 2000, *ApJ*, **537**, 368  
 Frontera, F., Costa, E., dal Fiume, D., et al. 1997, *SPIE*, **3114**, 206  
 Grindlay, J., Gursky, H., Schnopper, H., et al. 1976, *ApJL*, **205**, L127  
 Hasinger, G., & van der Klis, M. 1989, *A&A*, **225**, 79  
 Hirano, T., Hayakawa, S., Nagase, F., Masai, K., & Mitsuda, K. 1987, *PASJ*, **39**, 619  
 Kaaret, P., Piraino, S., Bloser, P. F., et al. 1999, *ApJL*, **520**, L37  
 Krimm, H. A., Markwardt, C. B., Still, M. D., et al. 2009, *ATel*, **2071**, 1  
 Kuśmierk, K., Madej, J., & Kuulkler, E. 2011, *MNRAS*, **415**, 3344  
 Kuulkler, E., den Hartog, P. R., in't Zand, J. J. M., et al. 2003, *A&A*, **399**, 663  
 Kuulkler, E., & van der Klis, M. 2000, *A&A*, **356**, L45  
 Lin, D., Remillard, R., & Homan, J. 2007, *ApJ*, **667**, 1073 (LRH07)  
 McConnell, M. L., Zdziarski, A. A., Bennett, K., et al. 2002, *ApJ*, **572**, 984  
 Migliari, S., Fender, R. P., Rupen, M., et al. 2004, *MNRAS*, **351**, 186  
 Morrison, R., & McCammon, D. 1983, *ApJ*, **270**, 119  
 Ng, C., Daz, T. M., Cadolle, B. M., & Migliari, S. 2010, *A&A*, **522**, A96  
 Parmar, A. N., Martin, D. D. E., Bavdaz, M., et al. 1997, *A&AS*, **122**, 309  
 Parsignault, D. R., & Grindlay, J. E. 1978, *ApJ*, **225**, 970  
 Piraino, S., Santangelo, A., Ford, E. C., & Kaaret, P. 1999, *A&A*, **349**, L77  
 Piraino, S., Santangelo, A., & Kaaret, P. 2000, *A&A*, **360**, 35  
 Priedhorsky, W., & Terrell, J. 1984, *ApJL*, **284**, L17  
 Rappaport, S., Nelson, L. A., Ma, C. P., & Joss, P. C. 1987, *ApJ*, **322**, 842  
 Seifina, E., & Titarchuk, L. 2011, *ApJ*, **737**, 128 (ST11)  
 Seifina, E., & Titarchuk, L. 2012, *ApJ*, **747**, 99 (ST12)  
 Seifina, E., Titarchuk, L., & Frontera, F. 2013, *ApJ*, **766**, 63  
 Shakura, N. I., & Sunyaev, R. A. 1973, *A&A*, **24**, 337  
 Shaposhnikov, N., & Titarchuk, L. 2004, *ApJL*, **606**, L57  
 Shaposhnikov, N., & Titarchuk, L. 2009, *ApJ*, **699**, 453  
 Simon, V. 2003, *A&A*, **405**, 199  
 Smale, A. P., Dotani, T., Mitsuda, K., & Zylstra, G. 1994, *BAAS*, **26**, 872  
 Smale, A. P., Zhang, W., & White, N. E. 1997, *ApJL*, **483**, L119  
 Stella, L., White, N. E., & Priedhorsky, W. 1987, *ApJL*, **315**, L49  
 Strohmayer, T., & Bildsten, L. 2004, in *Compact Stellar X-Ray Sources*, ed. W. H. G. Lewin & M. van der Klis (Cambridge Astrophysics Series 26; Cambridge: Cambridge Univ. Press), 113  
 Strohmayer, T. E., & Brown, E. F. 2002, *ApJ*, **566**, 1045  
 Sunyaev, R. A., & Titarchuk, L. G. 1980, *A&A*, **86**, 121  
 Tarana, A., Bassano, A., Ubertino, P., & Zdziarski, A. A. 2006, *ApJ*, **654**, 494  
 Titarchuk, L., Lapidus, I. I., & Muslimov, A. 1998, *ApJ*, **499**, 315  
 Vacca, W. D., Lewin, W. H. G., & Paradijs, J. 1986, *MNRAS*, **220**, 339  
 van Paradijs, J. 1978, *Natur*, **274**, 650  
 van Straaten, S., van der Klis, M., & Méndez, M. 2003, *ApJ*, **596**, 1155  
 Wardziński, G., Zdziarski, A. A., Gierliński, M., et al. 2002, *MNRAS*, **337**, 829  
 Wen, L., Levine, A. M., Corbet, R. H. D., & Bradt, H. V. 2006, *ApJS*, **163**, 372  
 White, N. E., Peacock, A., Hasinger, G., et al. 1986, *MNRAS*, **218**, 129  
 Wijnands, R., van der Klis, M., & Rijkhorst, E. J. 1999, *ApJL*, **512**, L39  
 Zdziarski, A. A., Wen, L., & Gierlinski, M. 2007, *MNRAS*, **377**, 1006  
 Zhang, W., Smale, A. P., Strohmayer, T. E., & Swank, J. H. 1998, *ApJL*, **500**, L171